

1 Mapping protein conformational landscapes from 2 crystallographic drug fragment screens

3
4 *Ammaar A. Saeed¹, Margaret A. Klureza², and Doeke R. Hekstra^{1,3*}*

5 ¹Department of Molecular & Cellular Biology, Harvard University, Cambridge, MA 02138

6 ²Department of Chemistry & Chemical Biology, Harvard University, Cambridge, MA 02138

7 ³School of Engineering & Applied Sciences, Harvard University, Cambridge, MA 02138

8 *Corresponding author. Email: doeke_hekstra@harvard.edu

9
10 **Keywords:** Conformational landscape, PCA, crystallographic drug fragment screen, PTP-1B,

11 MPro

12

13 **Abstract**

14 Proteins are dynamic macromolecules. Knowledge of a protein's thermally accessible

15 conformations is critical to determining important transitions and designing therapeutics.

16 Accessible conformations are highly constrained by a protein's structure such that concerted

17 structural changes due to external perturbations likely track intrinsic conformational transitions.

18 These transitions can be thought of as paths through a conformational landscape.

19 Crystallographic drug fragment screens are high-throughput perturbation experiments, in which

20 thousands of crystals of a drug target are soaked with small-molecule drug precursors

21 (fragments) and examined for fragment binding, mapping potential drug binding sites on the

22 target protein. Here, we describe an open-source Python package, COLAV (CONformational

23 LANDscape Visualization), to infer conformational landscapes from such large-scale

24 crystallographic perturbation studies. We apply COLAV to drug fragment screens of two

25 medically important systems: protein tyrosine phosphatase 1B (PTP-1B), which regulates insulin

26 signaling, and the SARS CoV-2 Main Protease (MPro). With enough fragment-bound structures,
27 we find that such drug screens also enable detailed mapping of proteins' conformational
28 landscapes.

29

30 **Introduction**

31 While often shown as single structures, proteins exhibit dynamic behavior necessary for their
32 function¹⁻³, e.g. binding and releasing ligands⁴, modulating activity⁵, and reversibly shielding the
33 active site⁶. Hence, proteins are better thought of as populating ensembles of structural states or
34 conformations. Individual protein molecules transition frequently between these conformations
35 through the concerted motions of their amino acids. For many proteins, there are only a handful
36 of accessible backbone conformations at physiological temperatures, all separated by distinct
37 concerted motions^{2,7}.

38

39 Consequently, proteins can often be thought of as residing on a conformational landscape that
40 describes metastable conformations and the concerted motions necessary to transition between
41 them⁸. Ideally, conformational landscapes would be inferred from experimental structures and
42 would succinctly recapitulate the known conformational diversity of a target protein.

43 Additionally, these empirical landscapes would suggest thermally accessible concerted motions
44 between conformations—probable temporal sequences of conformational change sometimes
45 referred to as conformational reaction coordinates or transition paths⁹⁻¹¹. Such conformational
46 landscapes for validated protein drug targets would suggest particular conformations to
47 (de)stabilize to enhance or inhibit functional activity. These conformations can then be targeted

48 by the design of a small molecule that binds the drug target within the active site (orthosteric) or
49 elsewhere (allosteric).

50
51 Existing biophysical methods can experimentally characterize aspects of a protein's
52 conformational landscape, e.g., by nuclear magnetic resonance (NMR) spectroscopy¹²,
53 fluorescence resonance energy transfer spectroscopy¹³, electron paramagnetic resonance
54 spectroscopy¹⁴, and room-temperature X-ray crystallography^{6,15}. These techniques probe the
55 equilibrium distribution of a desired conformational ensemble. However, such measurements
56 generally reflect the ground state of the protein and only provide limited insight into the presence
57 and/or nature of any alternate, higher-energy conformations. For large proteins and protein
58 complexes, cryogenic electron microscopy (cryo-EM) and electron tomography (cryo-ET) can
59 capture small populations of metastable conformations directly¹⁶, and machine learning methods
60 are beginning to pave the way for the identification of these rare protein states^{17,18}. Yet,
61 determining high-resolution structures of metastable states through cryo-EM or cryo-ET remains
62 an ongoing challenge, due to the need for a vast quantity of correctly classified particle images.

63
64 An alternative approach to studying these excited states is to directly perturb the protein of
65 interest. These perturbations alter the conformational landscape, stabilizing otherwise short-lived
66 excited states. Common methods to introduce perturbations include mutation of the protein and
67 addition of substrate/transition-state analogs. Once the protein has been perturbed, the stabilized
68 states can be examined via standard biophysical techniques. Though the efficacy of this approach
69 has been demonstrated in a variety of model systems¹⁹⁻²¹, designing individual perturbations can
70 be time-consuming and may only explore a limited portion of the conformational landscape.

71
72 An ideal approach to mapping protein conformational landscapes would be to subject the protein
73 of interest to a large number of distinct perturbations that are just strong enough to bias the
74 energetics of particular conformations by a few $k_B T$ and then determine the structure of the
75 protein under each perturbation^{22,23}. Crystallographic drug fragment screens constitute an
76 intriguing approximation to this ideal experiment: in these high-throughput crystallographic
77 screens, many crystals of the same drug target are each soaked with a unique drug fragment and
78 are then subjected to the standard X-ray crystallography pipeline. Advances in automation at the
79 Diamond Light Source²⁴ and elsewhere, paired with novel data processing software^{25,26}, have
80 enabled these screens to solve thousands of protein structures within days, some of which
81 contain bound drug fragments. Importantly, these drug fragment screens may yield information
82 valuable for drug design beyond the immediate identification of drug fragment/binding site pairs:
83 a comprehensive exploration of the protein's conformational landscape.

84
85 To test this idea, we developed a software package known as COLAV (CONformational
86 LANDscape Visualization) that calculates three different representations of protein structure—
87 dihedral angles, pairwise distances, and strain—to quantify structural change across a group of
88 crystal structures. COLAV is an open-source, Python-based software, freely available at
89 <https://github.com/Hekstra-Lab/colav>. Using COLAV, we show that sets of crystal structures can
90 be used to construct a map of a protein's conformational landscape and infer correlated regions
91 within the protein. We then ask whether the conformational landscape constructed from
92 structures obtained only from a crystallographic drug fragment screen is consistent with a map of
93 the landscape based on structures obtained using a variety of perturbations (e.g., mutants,

94 substrate analogs, and inhibitors) available from the Protein Data Bank (PDB)²⁷. We find that the
95 drug fragment-derived map provides a partial view of the conformational landscape that is
96 consistent with the landscape derived from the complete dataset. The drug fragment-derived map
97 becomes substantially more complete with increasing scale of the crystallographic drug fragment
98 screen.

99

100 **Methods**

101 *Structural representations*

102 We implemented three methods to represent a protein structure in COLAV: backbone dihedral
103 angles (ϕ , ω , and ψ), pairwise distances between C α atoms, and strain. We implemented these
104 methods on top of the Scientific Python stack (NumPy²⁸, SciPy²⁹, and BioPandas³⁰). Dihedral
105 angles and distances were calculated according to standard methods, and strain was calculated
106 according to previously published frameworks^{31,32} described briefly below. To ensure consistent
107 features across each protein dataset, we truncated structures at the N and C termini and then
108 removed any structures missing backbone atoms between the truncated endpoints. For PTP-1B,
109 we calculated representations between residues 7 and 279 (inclusive). For “focused PCA” of the
110 PTP-1B L16 loop, we only used representations between residues 236 and 244 (inclusive). For
111 MPro, we calculated representations between residues 3 and 297 (inclusive). If alternate
112 conformations had been modeled for any atoms, then we included only the “A” conformer in our
113 calculations. In our strain implementation, we calculated three different variants of strain: strain
114 tensor, shear tensor, and shear energy. We used the off-diagonal elements of the shear tensor as
115 inputs for principal component analysis (PCA). Use of COLAV is illustrated in the
116 accompanying Jupyter Notebooks available at <https://github.com/Hekstra-Lab/colav>.

117

118 *Data analysis*

119 We analyzed these structural representations using the Scikit-Learn implementation of PCA,
120 using 10 principal components (PCs) and otherwise default parameters³³. Because of the inherent
121 periodicity present in dihedral angles, we linearized these features by calculating the sine and
122 cosine of each angle and using the resulting tuple as the input feature for PCA. To determine a
123 per-residue measure of importance for each method (“residue contributions”), we transformed
124 the coefficients of the principal components as follows. For dihedral angles, we first summed the
125 absolute values of the sine and cosine coefficients of the same dihedral angle to determine a per-
126 angle, per-residue measure. We also summed the absolute values of these per-angle measures
127 into a single per-residue measure. For the pairwise distance representation, we summed the
128 absolute value of all coefficients pertaining to each residue. For the strain-based representation,
129 we summed the absolute value of the off-diagonal elements of the shear matrix for each residue.

130

131 We also analyzed these structural representations using the Scikit-Learn implementation of t-
132 distributed Stochastic Network Embedding³⁴ (t-SNE) and the Umap-Learn implementation of
133 Uniform Manifold Approximation and Projection³⁵ (UMAP). We initialized both of these latter
134 methods randomly; we did not observe major differences in the clustering of structures when
135 using different seeds. To identify groupings of structures similar to each other in the MPro
136 dataset, we used the Scikit-Learn implementation of the *k*-means algorithm with default
137 settings³³. In our assessment of the role of dataset size, we generated MPro datasets of varying
138 size by sampling the complete MPro dataset (without replacement) each time.

139

140 To establish the coupling between regions of PTP-1B, we performed Fisher exact tests for
141 independence (<https://www.socscistatistics.com/tests/>). This test asserts as a null hypothesis that
142 the variables used are independent and as an alternative hypothesis that there is a dependence
143 structure among the variables. We tested for conditional independence by adding the chi-square
144 statistics of two two-way tests and comparison to the null distribution (chi-square with two
145 degrees of freedom) as described in Ch. 5, “Analysis of Discrete Data”,
146 (<https://online.stat.psu.edu/stat504/book/>).

147

148 *Dataset construction*

149 For PTP-1B, we retrieved 165 structures of the human enzyme from the Protein Data Bank
150 (PDB) in March 2022 with a sequence identity of 90% or higher compared to wild-type PTP-1B.
151 We also retrieved 187 structures of PTP-1B bound to fragment ligands from a crystallographic
152 drug fragment screen³⁶ that were identified either by Pan-Dataset Density Analysis (PanDDA)²⁵
153 alone or after tandem processing by cluster4x²⁶ and PanDDA. We retrieved all PTP-1B files in
154 the PDB file format (hereafter .pdb).

155

156 For MPro, we retrieved all 1,830 crystallographic drug fragment screen structures in March 2022
157 from the Fragalysis database³⁷⁻⁴¹. We retrieved all 1,015 other MPro structures from the PDB in
158 July 2023. We excluded MPro structures from an ensemble refinement study of MPro at multiple
159 temperatures (7MHL, 7MHM, 7MHN, 7MHO, 7MHP, 7MHQ)⁴²; these temperature-induced
160 effects dominated the analysis, masking the native conformational landscape of MPro. Several
161 MPro structures were too large to download in the .pdb format, so we downloaded them in the

162 mmCIF file format. We subsequently converted them to the .pdb format using an online GEMMI
163 tool⁴³.

164
165 Before feature extraction, we aligned structures of PTP-1B or MPro using THESEUS v3.3.0⁴⁴, as
166 superposing structures of the same protein was crucial for proper strain calculations. Where
167 noted, we also idealized the backbone dihedral angles of each structure separately using
168 Representation of Protein Entities (RoPE)⁴⁵.

169

170 **Results and Discussion**

171 *A framework for examining conformational change*

172 COLAV offers three different structural representations to summarize differences between
173 conformations, each with a distinct emphasis (Table S1 summarizes the functions available in
174 COLAV). Dihedral angles and pairwise distances are internal coordinates, meaning that they are
175 measures calculated from atomic coordinates regardless of the orientation of the protein.

176 Therefore, these calculations can be performed on individual structures and do not require
177 alignment of protein structures. Dihedral angles efficiently summarize local backbone dynamics
178 of individual residues or loops by capturing these motions in only a few features, while pairwise
179 distances better capture global protein dynamics, such as breathing motions⁶.

180

181 In contrast, strain analysis is a directional measure of the structural deformations accompanying
182 conformational transitions. Using the strain analysis framework of previous studies^{31,32}, all the
183 structures must be aligned and compared to a designated reference structure. Here, the notion of
184 continuous strain is discretized, instead focusing on individual atoms and their surrounding

185 atomic neighborhoods—nearby atoms within 8 Å. By comparing the atomic neighborhoods in
186 the working and reference structures, discrete analogs to continuous strain can be estimated,
187 which then describe directional deformations of the desired structure relative to the reference.
188 Notably, strain measurements pick up on regions with relative motion, for example around hinge
189 points, while ignoring rigid-body-like motion, e.g., within subdomains.

190

191 *COLAV representations distinguish between known PTP-1B conformations*

192 We applied all three methods implemented in COLAV to infer the conformational landscape of
193 protein tyrosine phosphatase 1B (PTP-1B) from crystal structures. PTP-1B is a validated drug
194 target for type II diabetes⁴⁶ and breast cancer^{46,47}, and has been implicated in Alzheimer's
195 disease⁴⁸. Although there has been major pharmacological interest in PTP-1B, no drugs targeting
196 PTP-1B have successfully made it through stage II clinical trials⁴⁹. One major reason is that the
197 PTP-1B active site is highly conserved across the protein tyrosine phosphatase family, making it
198 difficult to design competitive inhibitors without off-target effects *in vivo*^{50,51}. The PTP-1B
199 active site is also charged, limiting the effective availability of charged competitive inhibitors
200 that must cross a cell's plasma membrane⁵¹. For these reasons, there has been widespread interest
201 in allosterically targeting and modulating PTP-1B activity⁵². It is of particular interest, then, to
202 discover surface sites allosterically coupled with the active site^{36,53,54}.

203

204 To do so, we first analyzed a set of 352 crystal structures of PTP-1B obtained from the PDB (165
205 individual structures and 187 structures from a drug fragment screen performed by Keedy *et*
206 *al.*³⁶). Using principal component analysis (PCA), we found that each structural representation of
207 conformational change implemented in COLAV separated the conformations into the same four

208 clusters of distinct, known conformations (Fig. 1). These four conformations are described by the
209 conformational states of the WPD and L16 loops (WPD loop/L16 loop): open/open (Fig. 1a top-
210 left), open/closed (Fig. 1b bottom-left), closed/open (Fig. 1c top-right), and closed/closed (Fig.
211 1d bottom-right). For dihedral angles and strain, the first two PCs clustered these conformations
212 (Fig. 1a, c); for pairwise distances, the first and third PCs clustered these conformations (Fig. 1b;
213 PC2 determines regions with large motions relative to the rest of PTP-1B). We also applied two
214 non-linear dimensionality reduction methods, t-distributed stochastic network embedding (t-
215 SNE) and uniform manifold approximation and projection (UMAP), to the structural
216 representations. These methods similarly clustered PTP-1B structures (Fig. S1), indicating that
217 the PCA clusters were representative of the major groupings in the PTP-1B structures. We next
218 asked whether inconsistent refinement practices for the deposited structures and/or deviations
219 from ideal geometry in individual structures could explain the observed structural heterogeneity.
220 To examine this possibility, we repeated the analysis after applying Representation of Protein
221 Entities (RoPE)⁴⁵ to all the PTP-1B structures to idealize and standardize the bond distances and
222 bond angles across the dataset. In RoPE, the backbone dihedral angles of the structures are
223 adjusted to match the original atomic coordinates. PCA identified the same PTP-1B clusters after
224 pre-processing the data (Fig. S2a, b, e), confirming that individual refinement artifacts did not
225 meaningfully affect the results.

226

227 The three different structural representations implemented in COLAV can each capture different
228 aspects of conformational change. It is conceivable that local conformational changes take place
229 without much global change and are therefore primarily detectable by monitoring dihedral
230 angles. Another possibility is that global change can be related to only a few dihedral angles,

231 e.g., in hinge motion, but be detectable elsewhere as changing distances to other parts of the
232 protein. Lastly, it is possible that coupled conformational changes are separated by regions of
233 almost imperceptible change—possibly a common case for proteins⁵⁵⁻⁵⁷. To compare the
234 conformational changes revealed by each representation, we calculated residue contributions
235 (RCs) from the coefficients of each of the principal components (PCs), combining per residue
236 the contributions of the sines and cosines of the dihedral angles (for the dihedral angle
237 representation), of distances to all other residues (for the C α pairwise distance representation), or
238 off-diagonal components of the shear matrix (for the strain representation), respectively, as
239 described in the Methods. By calculating the correlation between these RCs for each pair of
240 representations (Figs. 1d-f, S3), we find that the residue contributions underlying PC1 and PC2
241 (“RC1” and “RC2”) for dihedral angles and for strain are strongly correlated (0.79 comparing
242 RC1s and 0.74 comparing RC2s), respectively. Both RC1 and RC2 of these two representations
243 show a correlation with the residue contributions underlying PC1 and PC3 for pairwise distances
244 (Fig. 1d,f). As expected, however, the residue contributions are not perfectly correlated,
245 indicating differences in the aspects of conformational change captured by each representation.
246
247 The PCs distinguish conformational clusters by the states of the WPD loop (Fig. 2a, b; residues
248 176-188) and L16 loop (Fig. 2a-c; residues 237-243). The active-site WPD loop participates in
249 the PTP-1B catalytic mechanism, while the L16 loop is located ~15 Å away (Fig. 1a). Both loops
250 can take on open and closed states, and all four possible combinations of their states are present
251 in the existing crystal structures. These loops account for most of the conformational
252 heterogeneity present in the PTP-1B dataset (dihedral angles: 36.1% of total variance captured
253 by the first two principal components, C α pairwise distances: 66.6%, and strain analysis: 67.0%).

254 In the WPD loop-open state, the loop is positioned such that the active-site pocket is exposed,
255 facilitating substrate access and product release (Fig. 1a-left). In the WPD loop-closed state, the
256 loop binds the substrate and covers the active site pocket, facilitating catalysis⁴ (Fig. 1a-right).
257 The L16 loop states differ most saliently by the position of lysine 239 (K239)³⁶. In the open
258 state, the sidechain atoms of K239 interact primarily with the solvent (Fig. 1a-top). In the closed
259 state, the sidechain atoms of K239 interact with other residues in the protein (Fig. 1a-bottom). By
260 distinguishing the states of the WPD and L16 loops, PCA captures the major conformational
261 heterogeneity present in crystal structures of PTP-1B.

262
263 Could this conformational clustering be caused by crystal packing interactions, rather than the
264 effects of perturbations introduced in individual structures? The most common space group of
265 PTP-1B crystals in our dataset is the P₃₁2₁ space group, with 293 structures. The space groups of
266 other PTP-1B crystals are P₂₁2₁2₁ (29), P₁2₁1 (9), C₁2₁1 (9), P₃₂2₁ (7), and P₄₁2₁2 (2). As we
267 show in Figure S4, the set of structures from crystals in the P₃₁2₁, P₂₁2₁2₁, and P₁2₁1 space
268 groups each encompasses all four major conformational clusters. Only the two structures from
269 crystals in the P₄₁2₁2 space group take on only a single conformation (closed/open). Since PTP-
270 1B molecules across diverse space groups adopted different conformations, we conclude that
271 crystal packing artifacts cannot account for the conformational clusters highlighted by PCA.
272 Instead, these crystal structures represent semi-random samples from the PTP-1B conformational
273 landscape.

274

275 *COLAV enables detection of correlated regions in PTP-1B*

276 Although the crystal structures deposited in the PDB for any protein do not, together, constitute a
277 valid thermodynamic ensemble, there is a long history of interpreting frequencies observed in
278 crystal structures in thermodynamic terms⁵⁸⁻⁶¹, most recently extending to the interpretation of
279 AlphaFold parameters in energetic terms^{62,63}. In this spirit, the statistical correlations observed as
280 principal components can be interpreted as (rough) energetic couplings. Since the conformational
281 landscapes determined by PCA were equivalent for all structural representations, we focus here
282 on the dihedral angle representation (Fig. 1a). We interpreted the first principal component (PC),
283 which accounts for 29.7% of the total variance, to indicate a coupling between the WPD loop
284 and L16 loop (Fig. 2b). Indeed, previous experimental studies using multi-temperature X-ray
285 crystallography³⁶ and NMR^{53,54} have strongly suggested that these two loops are allosterically
286 coupled. We interpreted the second PC, which accounts for 6.3% of the variance, to indicate
287 additional motion of the L16 loop independent of the WPD loop (Fig. 2c). This observation
288 suggests two possibilities. Either the L16 loop undergoes two distinct motions—one coupled to
289 the WPD loop and another decoupled from the WPD loop—or the L16 loop undergoes a single
290 motion that is not always coupled to the WPD loop. To differentiate between these possibilities,
291 we performed a focused PCA on the dihedral angles of the L16 loop (Fig. 2d). We find that the
292 L16 loop has a single dominant motion (Fig. 2d-f) that distinguishes between the open and
293 closed states of the loop; this motion accounts for 63.5% of the variance in this focused PCA.
294 Thus, the L16 loop undergoes a single motion that is not always coupled to the WPD loop.

295
296 To examine this coupling more closely, we considered the confounding effect of the C-terminal
297 $\alpha 7$ helix, which has previously been implicated in allosteric coupling within PTP-1B⁵³ and forms
298 contacts with both loops in their respective closed states. We had initially excluded the $\alpha 7$ helix

299 from our analysis to avoid missing values, as the $\alpha 7$ helix can transition between an ordered,
300 folded helix state and a disordered state that is not crystallographically observable. However, we
301 noticed that the $\alpha 7$ helix typically takes on the ordered state when at least one of the WPD or L16
302 loops takes on their respective closed conformations (Table 1). We hypothesized that the
303 exclusion of the $\alpha 7$ helix had led to the observed inconsistencies in the coupling of the two loops.
304 Within the PTP-1B dataset, we find that the presence of an ordered $\alpha 7$ helix greatly increases the
305 probability of finding the closed state of each loop ($\sim 40x$ for the L16 loop and $\sim 50x$ for the WPD
306 loop). This suggests a cooperative mechanism in which binding of a ligand or inhibitor in the
307 active site can drive concerted loop closure and ordering of the $\alpha 7$ helix.

308
309 To formally test for a coupling between the three regions of PTP-1B, we performed a three-way
310 chi-square test of independence (Table 1; treating structures as independent observations),
311 finding strong evidence that these regions are not independent ($p \sim 10^{-158}$). To assess the role of
312 the $\alpha 7$ helix, we next tested how the correlation between the states of the WPD loop and L16
313 loop depends on the state of this helix (by Fisher's exact test). Given a disordered $\alpha 7$ helix, we
314 find no significant evidence for coupling of the WPD and L16 loops (however, the L16 loop is
315 rarely in the closed state when the $\alpha 7$ helix is disordered, limiting the power of this test). Given
316 an ordered $\alpha 7$ helix, the states of the two loops are strongly coupled to each other ($p = 0.006$;
317 Fisher's exact test). We can, in addition, reject the hypothesis that the state of the $\alpha 7$ helix solely
318 specifies the state of each loop, as the loop states are not conditionally independent given the
319 state of the $\alpha 7$ helix ($p = 0.005$; chi-squared test). Moreover, ligands are not necessary for the
320 protein to visit states with closed WPD and L16 loops and an ordered $\alpha 7$ helix. For instance, apo
321 structures collected at temperatures above 100 K (6B8E, 6B8T, 6B8X) show electron densities

322 consistent with both states at each of these regions. In addition, several mutations can stabilize
323 apo PTP-1B with the WPD and L16 loops in their closed states and an ordered $\alpha 7$ helix (1PA1,
324 6OLQ, 6OMY, 6PFW, 7KEN). The two loops are therefore coupled to each other and to the $\alpha 7$
325 helix, although the exact molecular mechanism remains unclear.

326

327 Detailed analysis of the COLAV results further showed active site deformation consistent with
328 oxidation of the active-site catalytic cysteine residue Cys215 (Fig. 3a,b). Oxidation dynamics of
329 this residue play a critical role in its function⁶⁴⁻⁶⁷ through a self-regulatory mechanism in PTP-
330 1B⁶⁵ and (when fully oxidized) degradation (Fig. 3a,b)⁶⁸. The most striking of several oxidized
331 states is a cyclized state in which a sulphenyl-amide bond between the S γ atom of Cys215 and
332 the backbone nitrogen atom of Ser216 forms a five-membered ring. Structures of oxidized
333 conformations (1OEM and 1OES) show deformations at active site loops, matching RC4
334 (accounted for 3.5% of total variance) and RC5 (accounted for 2.9% of total variance) of the
335 dihedral angle representation (Fig. 3d,e). Only six PTP-1B structures present in the dataset
336 (~2%) have oxidized cysteine states modeled, and PCA distinguishes these structures from
337 structures in the native, reduced state (Fig. 3c, top-right corner). However, it is possible that low
338 levels of oxidation in PTP-1B crystals are present more widely in the structures³⁶, impacting the
339 average electron density and, therefore, structure coordinates. Overall, applying PCA to COLAV
340 results successfully identified these rare conformations.

341

342 In the analysis of these oxidized structures, we further noticed a strong signal from a region of
343 PTP-1B distant from the active site and distinct from the L16 loop (green shaded box in Figure
344 3d,e). This spike in signal corresponds to a short loop including residues 59-66. Intriguingly, this

345 loop is near Ser50 and contains Tyr66, two known phosphorylation sites of PTP-1B^{69,70}.
346 Furthermore, a computational analysis of PTP-1B by CryptoSite⁷¹ indicated that this loop is
347 directly adjacent to a cryptic binding site capable of accommodating a small molecule. These
348 observations point to a potential regulatory role of this loop in PTP-1B and perhaps a more direct
349 role in the regulation of oxidized PTP-1B. Speculatively, recent work has shown that the E3-
350 ligase Cullin1 is known to interact with oxidized (sulfonated Cys215) PTP-1B, but the
351 mechanism of this molecular recognition is unclear. The putative coupling suggested by our
352 analysis implies that oxidation of Cys215 triggers concerted motions in this loop, which may
353 allow for recognition and ubiquitination by Cullin1.

354

355 *Drug fragment screen structures recapitulate the PTP-1B conformational landscape*

356 Could structures from only the PTP-1B crystallographic drug fragment screen³⁶ suffice to infer
357 the same conformational landscape as the complete PTP-1B dataset or the (non-screen) PTP-1B
358 structures deposited in the PDB (“PDB-only”)? To address this question, we again used the
359 dihedral angle representation to map the conformational landscape of PTP-1B based solely on
360 either the fragment screen or the PDB structures (Fig. 4). We first quantified the similarity of the
361 fragment screen-only dataset and the PDB-only dataset using matching and coverage scores^{72,73}.
362 The matching score reports on how similar the datasets are by RMSD (root-mean-square
363 deviation) and the score ranges from 0 (each structure has an identical match in the other dataset)
364 to infinity. The coverage score reports on the relative diversity between the datasets and ranges
365 between 0 and 1. Because these scores compare individual structures between datasets,
366 comparing either the fragment screen-only or the PDB-only datasets to the complete dataset
367 would yield perfect scores (matching score of 0 and coverage score of 1) because they contain

368 the same structures, so we compared the fragment screen-only dataset and PDB-only dataset. We
369 calculated the matching score to be 0.493 Å and the coverage score to be 0.963 with an RMSD
370 similarity cutoff of 1.0 Å, which indicated that the fragment screen-only dataset resembles the
371 PDB-only structures both in terms of containing similar (“matching”) structures and in the
372 overall coverage of the conformational landscape.

373
374 To determine the relationship between the inferred conformational landscapes more carefully, we
375 compared RCs for PCs from each dataset by calculating correlation coefficients. We found that
376 most key RCs from the complete dataset were also clearly identifiable from the fragment screen-
377 only dataset (Fig. 4a). We found similar results when we compared RCs of the fragment screen-
378 only dataset and the PDB-only dataset (Fig. 4b). This mapping suggests similar structural
379 interpretations for the complete, fragment screen-only, and PDB-only datasets. Indeed, the fifth
380 and seventh fragment screen RCs resemble the first and second RCs of the complete dataset,
381 again indicating a coupling between the WPD loop and L16 loop (Fig. 4c-e), albeit with different
382 proportions of the major states. We note that since refinement of partial-occupancy states, typical
383 for drug fragment screens, tends to be biased towards the unbound state, closed-loop
384 conformations are likely underreported. Effects of catalytic cysteine oxidation were more
385 prominent in the drug fragment screen than in the whole dataset, as observed by Keedy *et al.*³⁶,
386 such that the second and third fragment screen RCs correlated well with the fourth and fifth RCs
387 of the complete dataset. As discussed above, the fourth and fifth RCs of the complete dataset
388 report on active site deformation due to Cys-215 oxidation (Fig. 4f-h). We note that the first PC
389 of the fragment-only dataset partially reports on a coupling between the L16 loop and the K loop,
390 another active-site loop, that receives little weight in the PDB-only dataset (Fig. S5b). These

391 comparisons show that the PTP-1B fragment screen conformational landscape matches that of
392 the complete PTP-1B dataset, albeit with a different order of the PCs. This reordering reflects the
393 relative prevalence of the different conformations in the fragment screen dataset.

394

395 *Continuous motions in the SARS-CoV-2 linker may be coupled to distant surface sites*

396 We next applied the representations implemented in COLAV and PCA to the SARS-CoV-2
397 main/3CL protease (MPro). MPro is a component of a polyprotein translated from the positive-
398 sense SARS-CoV-2 RNA genome. Through its protease activity, MPro cleaves itself and other
399 functional proteins from this polyprotein, making MPro essential for viral replication⁷⁴.
400 Consequently, MPro is a validated drug target for coronavirus disease caused by SARS-CoV-2
401 infection (COVID-19). The protein consists of three subdomains: domains I and II form a β -
402 barrel catalytic core, and domain III forms an α -helical bundle unit that facilitates MPro obligate
403 homodimerization (Fig. 5a,b)^{75,76}. MPro is the subject of an intense research effort, with several
404 crystallographic drug fragment screens and many other structural studies capturing the
405 homodimer bound to a variety of ligands³⁷⁻⁴¹. We analyzed 1,830 structures from these fragment
406 screens and 1,015 other structures deposited in the PDB to determine the MPro conformational
407 landscape by PCA.

408

409 In contrast to PTP-1B, the MPro conformational landscape is dominated by a continuous band of
410 structures along PC1 rather than by distinct clusters (Fig. 5c); along PC2, there is a distinct
411 cluster of structures. We cautiously interpreted this to mean that the most common motions in
412 MPro are continuous in the protein: the most flexible regions of the protein do not take on
413 distinct, individual states. However, structures that are related in our conformational landscape, a

414 reduced-dimensional space, may be more dissimilar in the higher-dimensional space considering
415 all dihedral angles. To test this interpretation, we determined similar groups of MPro structures
416 using the k -means algorithm ($k = 8$) for the full high-dimensional dihedral angle representation of
417 each structure, yielding groups that are similar in the high-dimensional space. This proximity is
418 well preserved in the low-dimensional space of the first two principal components (Fig. 5c). As
419 for PTP-1B, PCA determined similar results for the three structural representations according to
420 the k -means groups (Fig. S6; coloring of the structures matches between panels; t-SNE and
421 UMAP analysis in Figure S6). From these analyses, we concluded that the dominant concerted
422 motion in MPro is a gradual deformation.

423

424 To further investigate the motions of MPro and its correlated regions, we examined the residue
425 contributions, again focusing on the dihedral angle representation. We interpreted the RCs
426 corresponding to PC1 and PC2, respectively accounting for 14.4% and 7.0% of the total
427 variance, as indicative of motion in the linker between domains II and III (Fig. 5d,e). Molecular
428 dynamics simulations and ensemble refinement of MPro structures have shown that this region
429 of the protein is flexible^{42,77}. In addition, the motion corresponding to the first PC indicates that
430 this linker is correlated with residues 148-154 and residues 215-227 (Fig. 5d,e). These regions
431 are located approximately 20 Å and 30 Å away from the linker, respectively, in both a single
432 protomer and the homodimer (Fig. 5a,b), indicating an allosteric coupling between these
433 regions. Because the linker abuts the MPro active site, these regions may be suitable targets for
434 drug design.

435

436 Next, we asked again whether the drug fragment screen recapitulates the conformational
437 landscape inferred from either the complete MPro dataset or the non-fragment screen (“PDB-
438 only”) dataset, as we did for PTP-1B above. We similarly find that the fragment screen-only
439 dataset is nearly as conformationally diverse as the PDB-only dataset, with a coverage score of
440 0.925 using a RMSD threshold of 1.0 Å; a matching score of 0.466 Å shows that the structures
441 of the fragment screen-only dataset closely match those of the PDB-only dataset. Likewise, we
442 similarly find that the residue contributions to the different PCs have close matches between the
443 fragment screen-only dataset and the whole dataset or the PDB-only dataset (Fig. S7). Therefore,
444 as in PTP-1B, COLAV analysis of the MPro crystallographic drug fragment screen mapped the
445 MPro conformational landscape efficiently and thoroughly.

446
447 We have found that conformational landscapes inferred from drug fragment screens alone
448 recapitulate the main features of the conformational landscapes that can be inferred from larger
449 ensembles of structures present in the PDB, often including deliberately designed mutants or
450 targeted ligands. The stronger correspondence found for MPro (Figure 5) than for PTP-1B
451 (compare Figure 4 to Figures 1-3) suggests that the sheer number of fragment-bound structures is
452 an important parameter. To test this idea, we generated random samples from the MPro drug
453 fragment screening dataset without replacement. We then compared the inferred conformational
454 landscapes (based on dihedral angles) to the complete dataset by calculating correlation
455 coefficients between RCs (Fig. S7). Compared to the complete dataset, we found that a reduced
456 dataset of 135 structures was sufficient to broadly capture the top 5 RCs of the complete dataset
457 (Fig. S7e). Most of the top 10 RCs were strongly recapitulated in the reduced datasets of 270 and

458 540 structures (Fig. S7c, d), matching the visual appraisal that the inferred conformational
459 landscape looks like that of the complete dataset.

460

461 *Ordering protein structures by PC score exposes potential transition pathways*

462 The PCA results showed several apparent conformational transitions in both PTP-1B and MPro.

463 To examine these transitions more closely, we used the PC scores to order the structures of either

464 PTP-1B or MPro for both PC1 and PC2 using the dihedral angle representation (Fig. 6). Doing

465 so with PC1 for PTP-1B showed a distinct transition of the WPD loop between the open and

466 closed state (Fig. 6a), while the same for PC2 described the transition of the L16 loop from a

467 closed to open state (Fig. 6b). For MPro, the transitions between most conformations for PC1

468 and PC2 are more subtle (Fig. 6c, d), except for a distinct transition between MPro

469 conformations in the linker along PC2 (Fig. 6d). Ordering structures by PC scores is especially

470 informative when analyzing structures from crystallographic drug fragment screens, as

471 conformations can be paired with the fragment ligands that stabilize them. Those fragment

472 ligands that stabilize particular conformations of the target protein are then readily identifiable as

473 the basis for targeted rational drug design.

474

475 **Conclusions**

476 Crystallographic drug fragment screens provide rich data, not only concerning the binding sites

477 of fragments on drug targets but also on how protein conformations change in response to such

478 binding. In this respect, drug fragment screens approximate an ideal experiment in which the

479 structure of a protein is determined in the presence of each of many random perturbations. We

480 introduced an open-source software package, COLAV, to facilitate inference of empirical

481 conformational landscapes from such drug fragment screening data using three different
482 representations of conformational change. We find that the results are insensitive to the choice of
483 representation and largely robust under the choice of method for dimension reduction, indicating
484 that the discovered conformational clustering is intrinsic to the conformational ensembles
485 studied. Moreover, we found that the conformational landscapes determined this way resemble
486 those inferred from the larger universe of previously determined structures and that the
487 correspondence improves with the number of fragment-bound structures. Altogether, these
488 findings lay the foundation for the systematic use of crystallographic drug fragment screens to
489 map the accessible states of proteins of interest and a roadmap for steering proteins toward
490 desirable conformations. The tools introduced in COLAV are general and may perform equally
491 well for other protein structural ensembles, as the highly constrained nature of protein dynamics
492 will leave its fingerprints on any such dataset.

493

494 **Author Contributions**

495 AAS, MAK, and DRH conceived the approach. AAS developed the code and performed the
496 analysis with feedback from MAK and DRH. All authors contributed to the manuscript.

497

498 **Funding Sources**

499 This work was supported by the Harvard College Research Program (to AAS) and the NIH
500 Director's New Innovator Award (DP2-GM141000 to D.R.H.).

501

502 **Acknowledgement**

503 We thank Dr. Daniel Keedy and Dr. Helen Ginn, and members of the Hekstra lab for fruitful
504 discussions. We thank Dennis Brookner for assistance in making COLAV available as a package
505 on <https://github.com/Hekstra-Lab/colav> and PyPI.

506

507 **Declaration of Interests**

508 The authors declare that no competing interests exist.

509

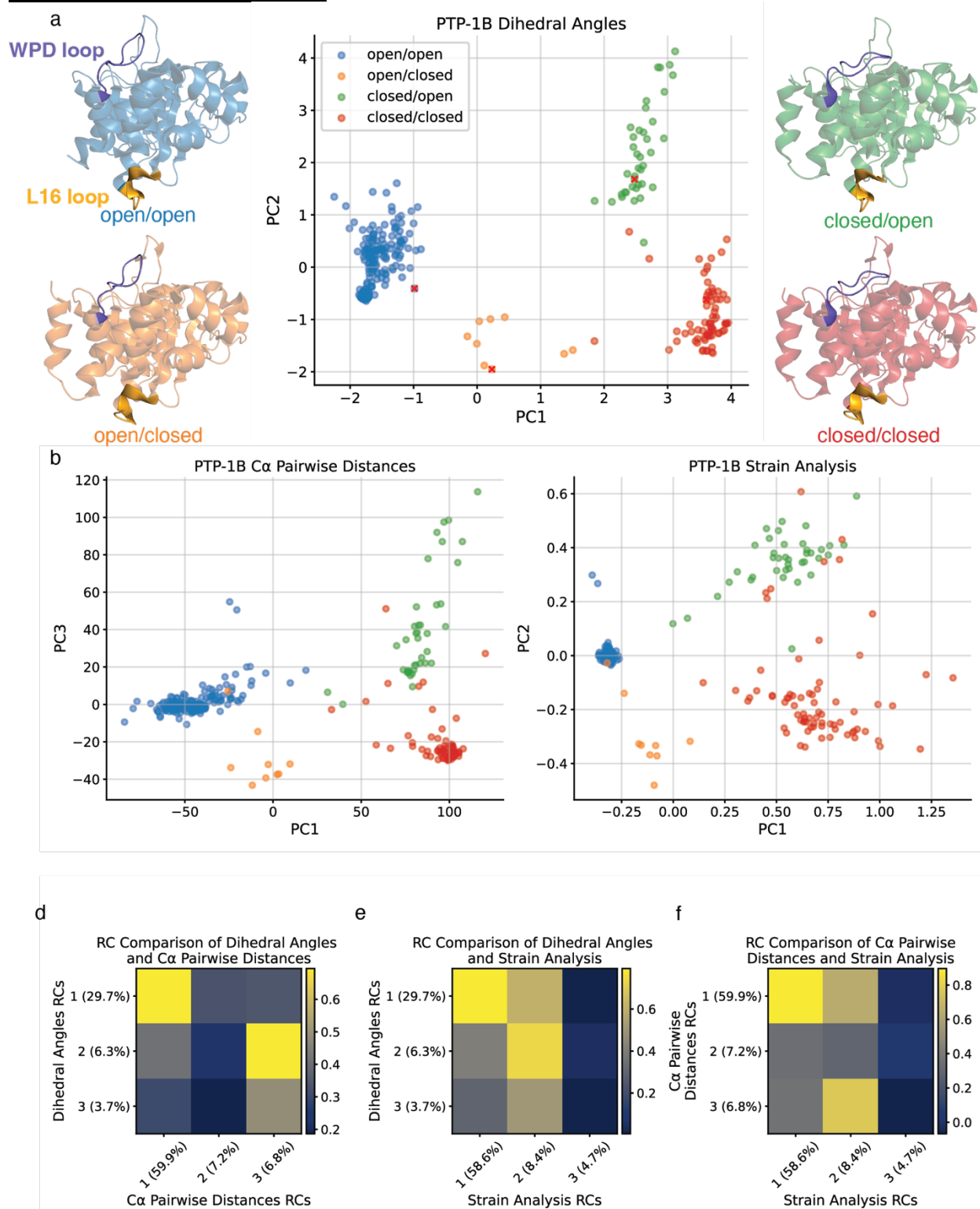
510 **Data and Code Availability**

511 All data and code used in this study to generate the figures can be found at
512 <https://github.com/Hekstra-Lab/colav>. Figures were prepared using PyMOL v2.5.4, available
513 from Schrödinger, LLC.

514

515

516 **Figures and Tables**
 517 **Figure 1 caption on next page**



518

Figure 1: Conformational landscape of PTP-1B inferred using three different structural representations and colored by conformation.

(a) PTP-1B conformational landscape by dihedral angles, flanked by representative PTP-1B structures of the four major conformations labeled by the conformational state of the WPD loop (purple) and L16 loop (yellow): (open/open: 1NWL, open/closed: 4QBW, closed/open: 1PXH, closed/closed: 1SUG). (b) PTP-1B conformational landscape by C α pairwise distances; note that PC3 is shown on the y-axis. (c) PTP-1B conformational landscape by strain analysis. (d-f) Correlation coefficient matrix comparing RCs 1-3 for (d) dihedral angles and C α pairwise distances; (e) dihedral angles and strain; (f) C α pairwise distances and strain.

519

520

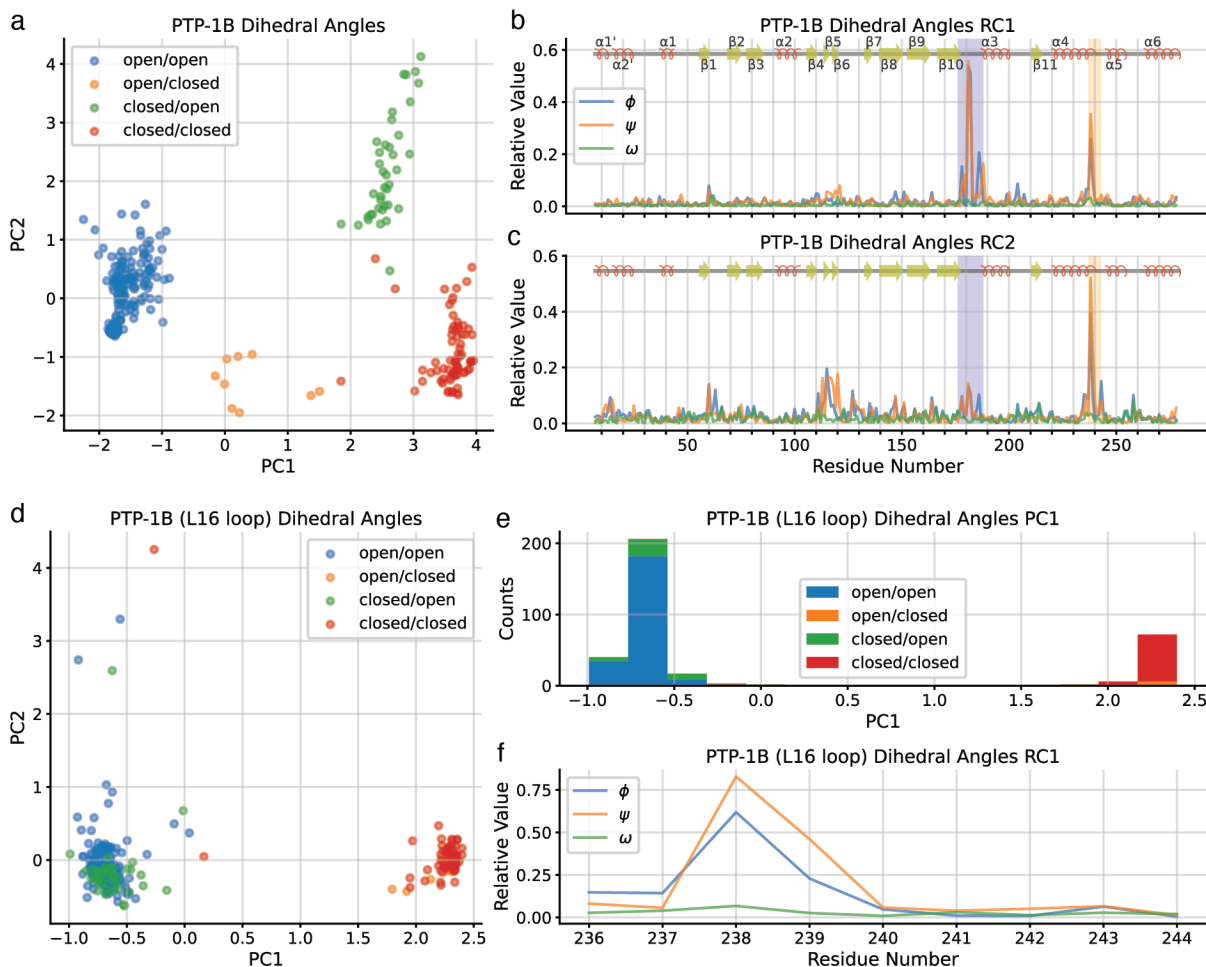


Figure 2: The dihedral angle representation distinguishes between conformations of PTP-1B based on the conformations of the WPD loop and L16 loop.

(a) PTP-1B conformational landscape by dihedral angles by PC1 and PC2. (b) Residue contributions to principal component 1 (PC1), with WPD loop (residues 176-188) indicated by a purple box and L16 loop (residues 237-243) in a yellow box. (c) Residue contributions to PC2, with WPD loop in purple box and L16 loop in yellow box. (d) PTP-1B L16 loop conformational landscape by dihedral angles colored by conformation. (e) Histogram of PTP-1B structures according to PC1 of the focused PCA. (f) Residue contributions to PC1 of the focused PCA.

521

522

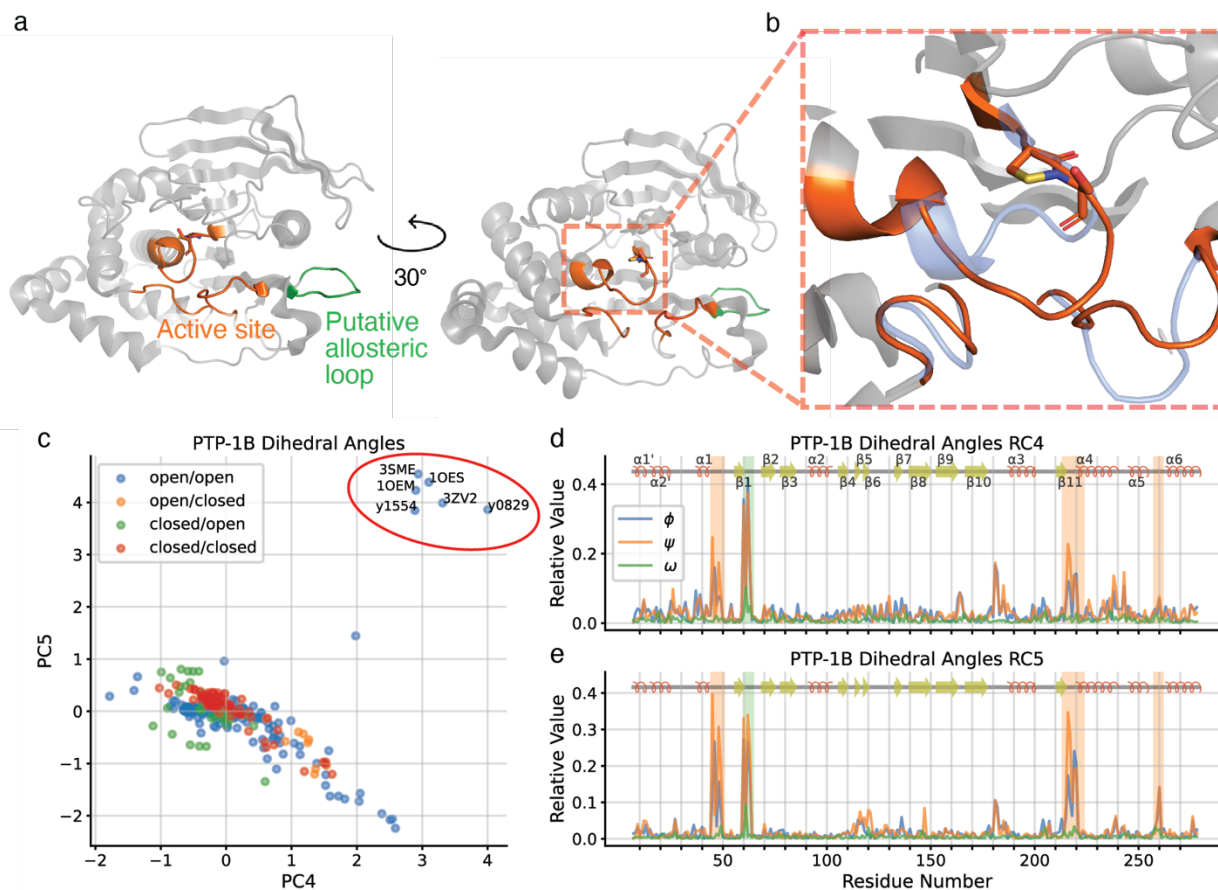
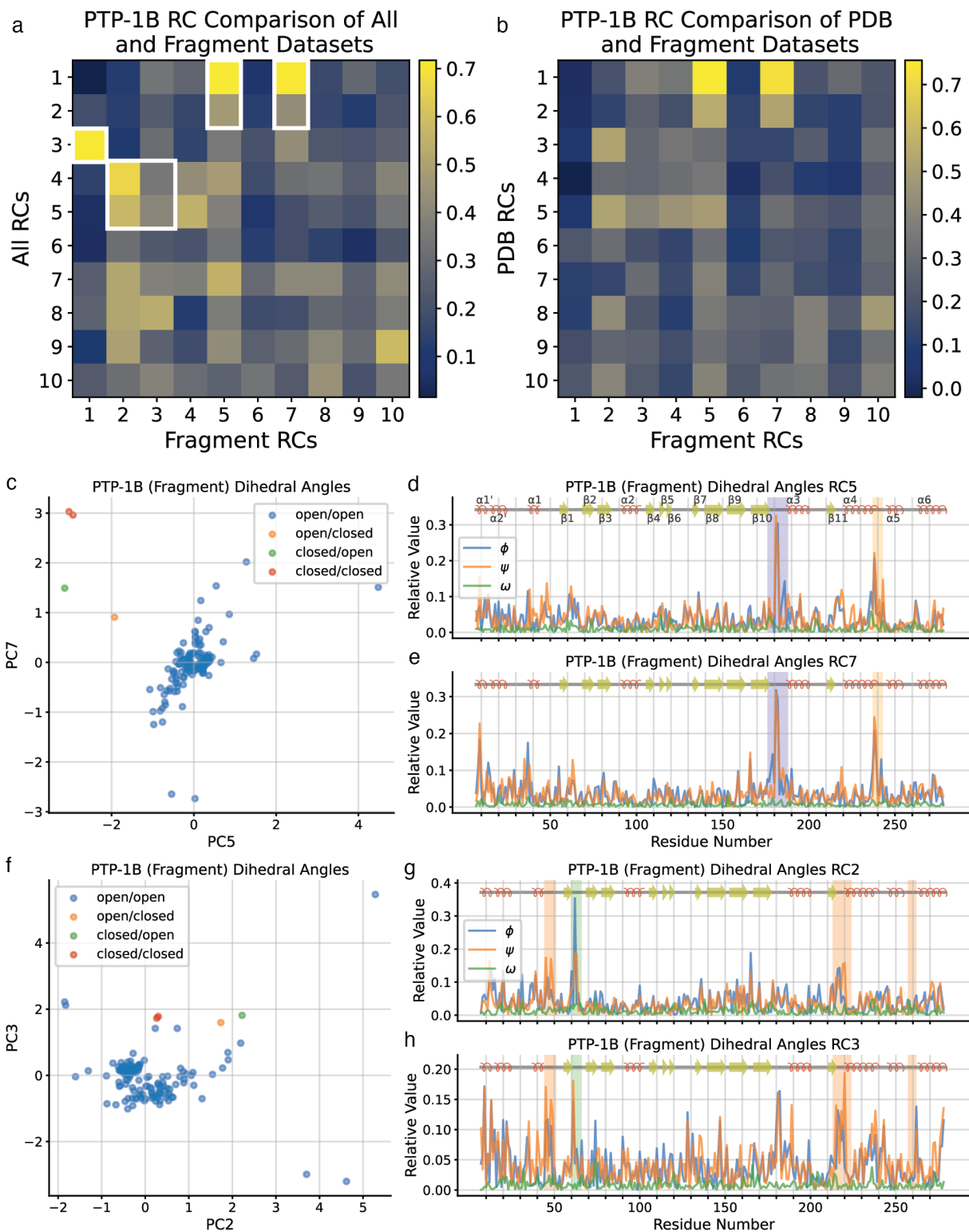


Figure 3: PTP-1B conformational change due to oxidation states of Cys215.

(a) Cartoon representations of oxidized PTP-1B conformation (1OES), highlighting active site loops (orange) and putative allosteric loop (green). (b) Cartoon representation of the oxidized PTP-1B active site conformation (1OES; orange), with sulphenyl-amide ring shown in sticks, and the reduced PTP-1B active site conformation (1SUG; blue) for comparison. (c) PTP-1B conformational landscape by dihedral angles by PC4 and PC5; structures showing oxidized PTP-1B conformation as in panels (a) and (b) are circled in red. (d) Residue contributions to PC4, with active site loops in orange box and putative allosteric loop (residues 59-66) in green box (coloring matches panel (a)). (e) Residue contributions to PC5, with loop coloring as in panel (d).

523

524



525 **Figure 4 caption on next page**

Figure 4: COLAV analysis of the PTP-1B crystallographic drug fragment screen recapitulates key aspects of the conformational landscape.

(a, b) Correlation coefficient matrix comparing residue contributions (RCs) of (a) the complete PTP-1B dataset to those of the fragment screen-only PTP-1B dataset, and (b) the PDB-only PTP-1B dataset to those of the fragment screen-only PTP-1B dataset. Correlations discussed in the text are highlighted using white edges. (c) Fragment screen PTP-1B conformational landscape by dihedral angles, emphasizing similarities of PC5 and PC7 with PC1 and PC2 of the complete PTP-1B conformational landscape. (d) Residue contributions to PC5, with WPD loop in purple box and L16 loop in yellow box. (e) Residue contributions to PC7, with coloring as in panel (d). (f) Fragment screen PTP-1B conformational landscape by dihedral angles, emphasizing similarities of PC2 and PC4 with PC4 and PC5 of the complete PTP-1B conformational landscape. (g, h) Residue contributions to (g) PC2 and (h) PC4, with active site loops in orange box and putative allosteric loop in dark blue box.

526
527
528
529
530

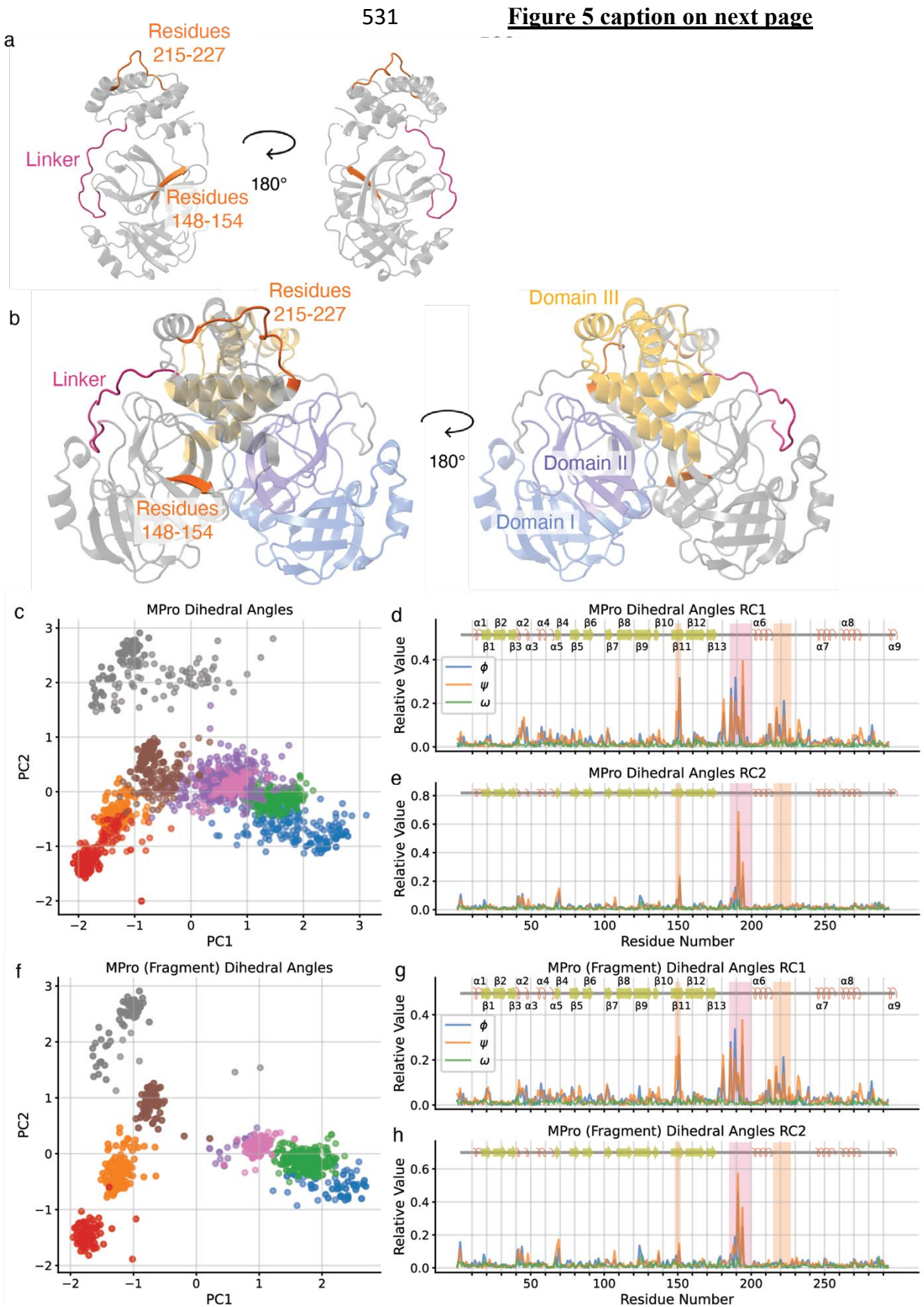


Figure 5: The MPro complete dataset and fragment-screen-only dataset generate similar conformational landscapes

(a) Cartoon representations of single MPro protomer (7AR5), highlighting linker (residues 185-200) in magenta and putative allosteric regions (residues 148-152 and 215-227) in orange. (b) Cartoon representations of MPro homodimer (7AR5), highlighting subdomain I in blue, subdomain II in purple, and subdomain III in yellow on protomer 1 and linker and putative allosteric regions colored as in (a). (c) MPro conformational landscape by dihedral angles. (d) Residue contributions to PC1, with linker in magenta box and putative allosteric loops in orange box (coloring matches panels (a) and (b)). (e) Residue contributions to PC2, with loop coloring as in panel (d). (f) Fragment screen MPro conformational landscape by dihedral angles. (g, h) Residue contributions to fragment screen (g) PC1 and (h) PC2, with loop coloring as in panel (d).

537

538

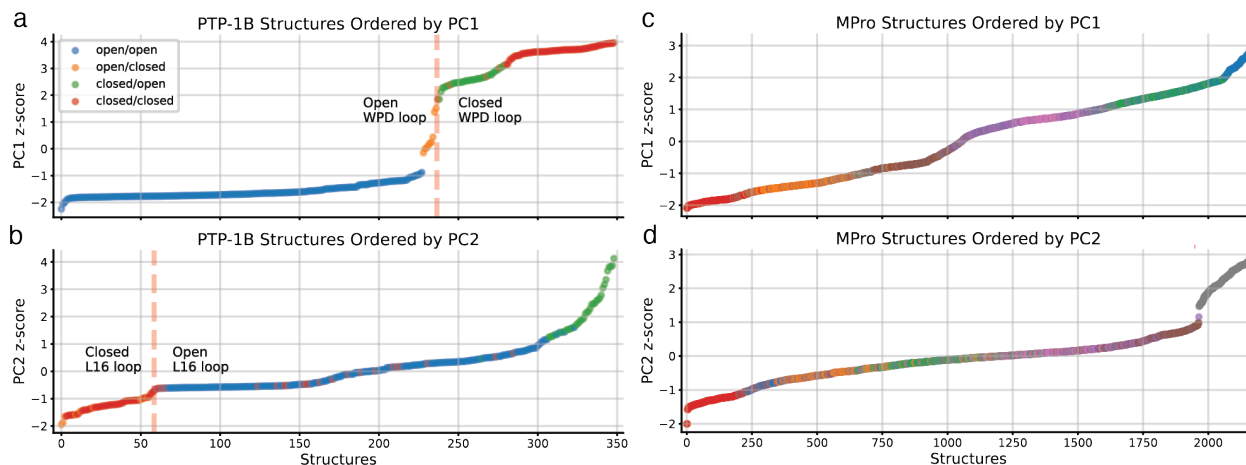


Figure 6: Ordering structures of PTP-1B and MPro by PC scores marks distinct conformational transitions.

(a) PTP-1B structures ordered by dihedral angle score along PC1, with the transition from open WPD loop to closed WPD loop highlighted. (b) PTP-1B structures ordered by dihedral angle score along PC2, with the transition from closed L16 loop to open L16 loop highlighted. (c) MPro structures ordered by dihedral angle score along PC1. (d) MPro structures ordered by dihedral angle score along PC2. Coloring of datasets for both proteins matches preceding figures.

539

540

Disordered $\alpha 7$ Helix

	Open L16	Closed L16	total
Open WPD	221	4	225
Closed WPD	23	1	24
total	244	6	249

P-value: 0.40

Ordered $\alpha 7$ Helix

	Open L16	Closed L16	total
Open WPD	7	5	12
Closed WPD	16	72	88
total	23	77	100

P-value: 0.006

541
542 **Table 1: Assessing the correlations of the WPD loop, L16 loop, and $\alpha 7$ helix through χ^2 test of independence.**
543 Contingency table comparing PTP-1B conformations of the WPD loop, the L16 loop, and the $\alpha 7$ helix. Calculated p-
544 values are based on a Fisher exact test.
545
546
547
548

Protein	Matching Score (\AA)	Coverage Score
PTP-1B	0.493	0.963
MPro	0.466	0.925

549 **Table 2: Matching and coverage scores comparing PDB-only and fragment screen-only structures for PTP-1B**
550 **and MPro.**
551 The matching score reports on the similarity of the datasets by RMSD, and a smaller score implies that the datasets
552 are more similar. The coverage score reports on diversity of structures between datasets, and the highest score of 1
553 implies that the datasets are similarly diverse.
554
555

556 **Supplementary Figures and Table**

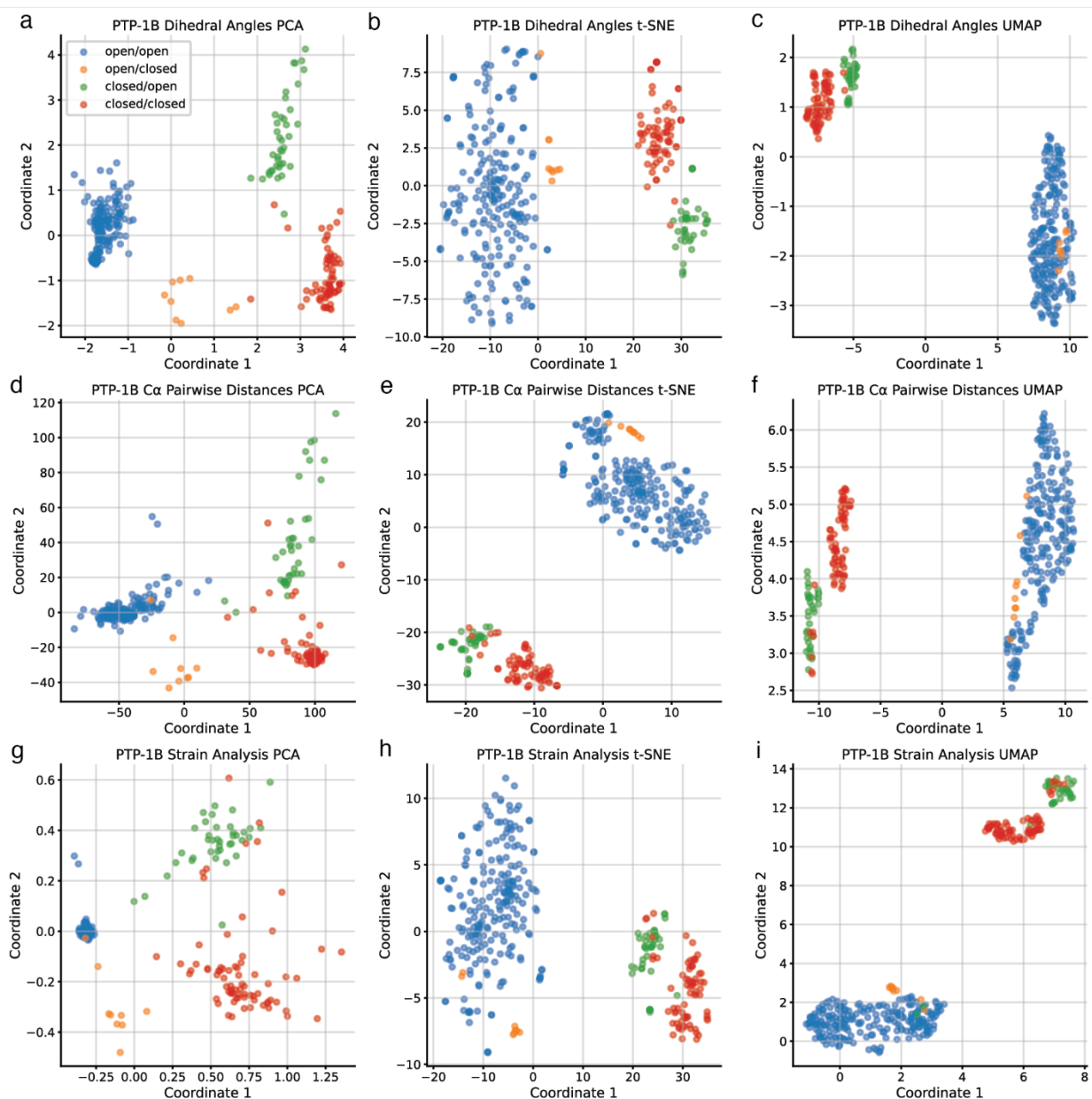


Figure S1: Comparison of PCA, t-SNE, and UMAP applied to all three structural representations of PTP-1B colored by conformation.

(a-c) PTP-1B conformational landscape based on dihedral angles with dimensionality reduction by (a) PCA, (b) t-SNE, and (c) UMAP. (d-f) PTP-1B conformational landscape based on C α pairwise distances, analyzed using (d) PCA, (e) t-SNE, and (f) UMAP. (g-j) PTP-1B conformational landscape based on strain analysis and (g) PCA, (h) t-SNE, and (i) UMAP. Coloring of structures is consistent among all panels.

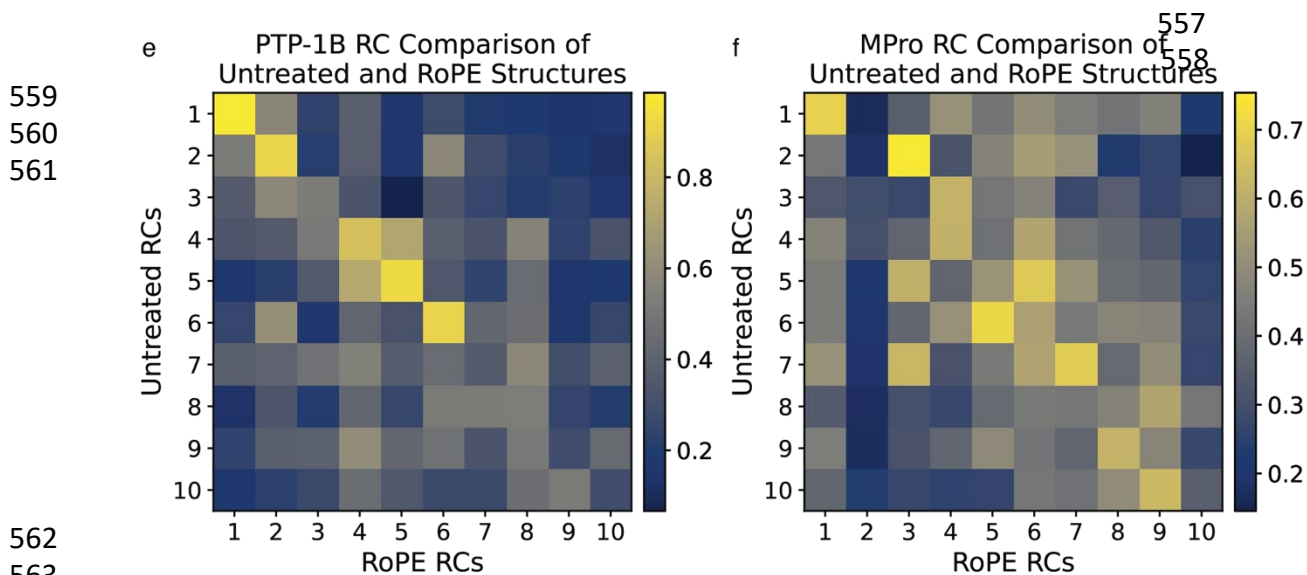
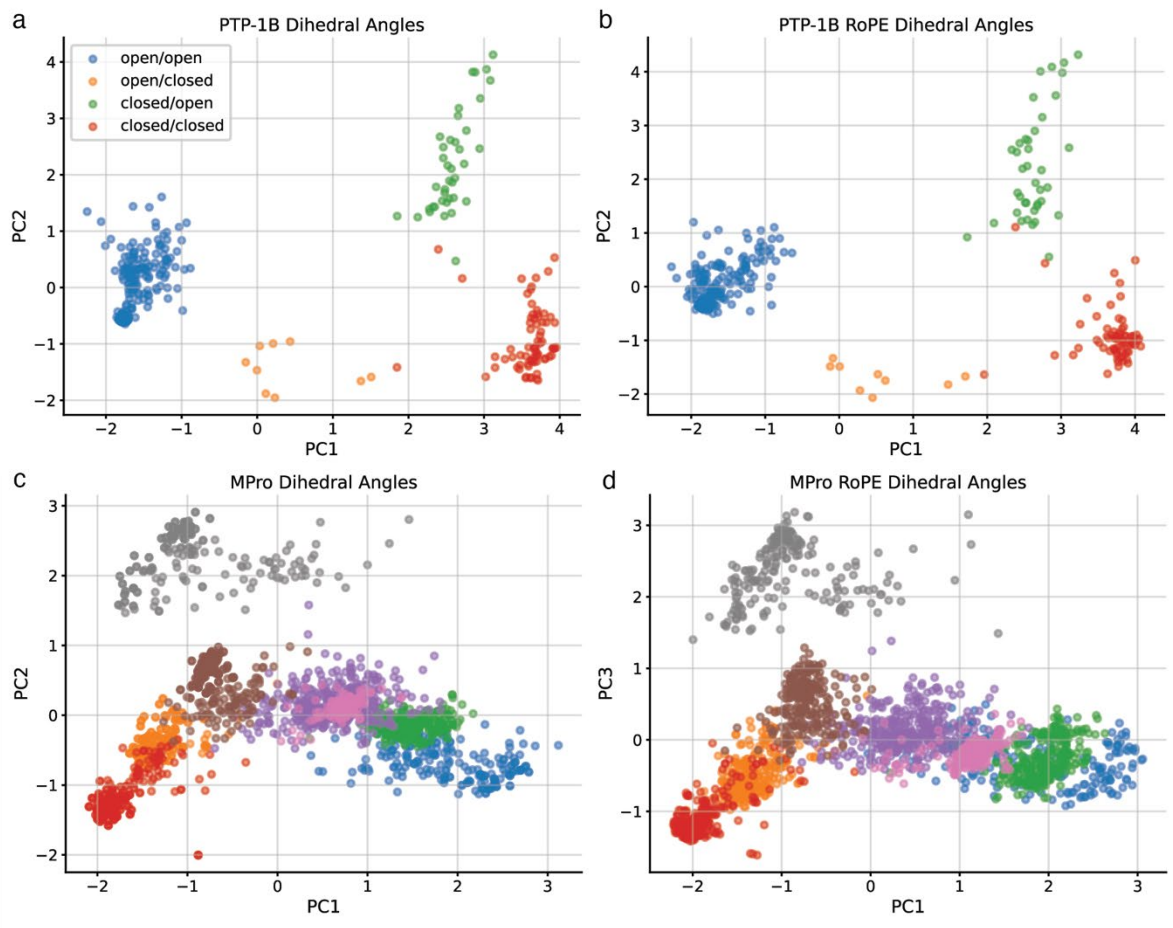


Figure S2 caption on next page

Figure S2: Dihedral angles with and without idealization by RoPE reveal similar conformational landscapes.

(a) PTP-1B conformational landscape by dihedral angles calculated by COLAV. (b) PTP-1B conformational landscape by dihedral angles idealized by RoPE. (c) MPro conformational landscape by dihedral angles calculated by COLAV. (d) MPro conformational landscape by dihedral angles calculated by RoPE. (e) Correlation coefficient matrix comparing PTP-1B RCs of the untreated (COLAV) dihedral angles and RoPE dihedral angles. (f) Correlation coefficient matrix comparing MPro RCs of the untreated (COLAV) dihedral angles and RoPE dihedral angles.

565

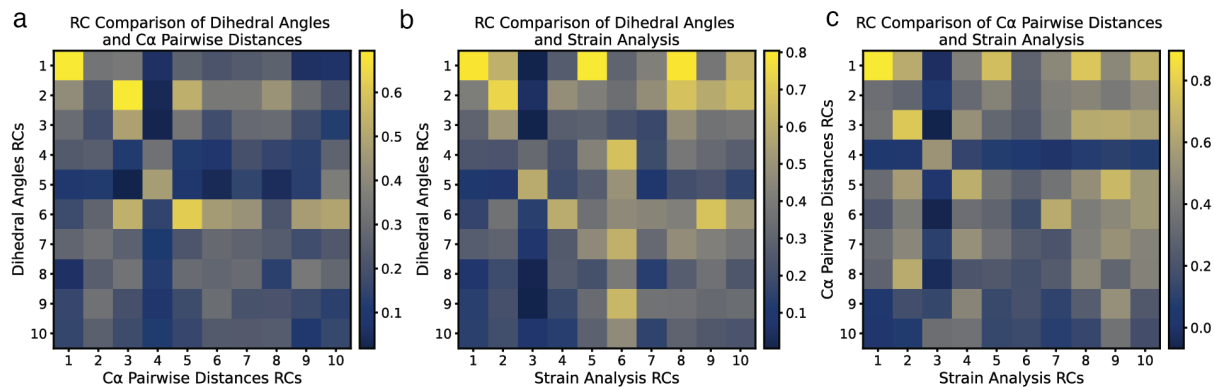


Figure S3: Comparison of residue contributions for structural representations of PTP-1B.

Correlation coefficients comparing PTP-1B residue contributions (RCs) for (a) dihedral angles and Cα pairwise distances, (b) dihedral angles and strain, and (c) Cα pairwise distances and strain.

566

567

568

569

570
571

572

573

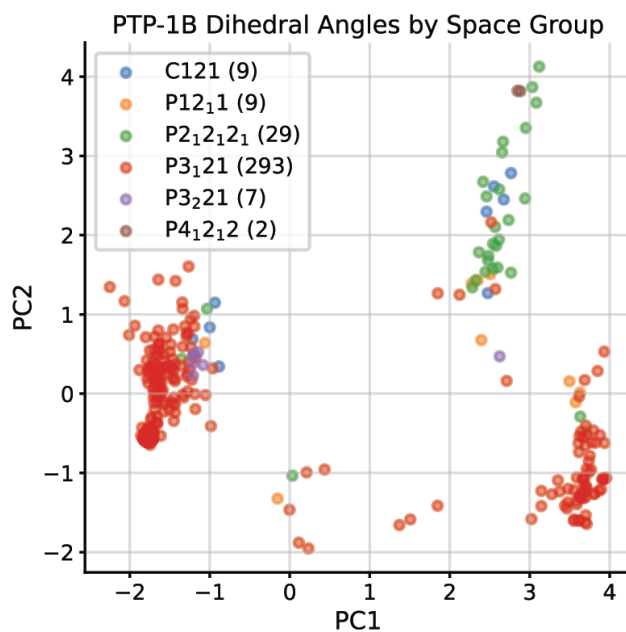


Figure S4: PTP-1B conformations are found across space groups.

Distribution of structures of PTP-1B after PCA of their dihedral angles. Structures are colored by the space group of their crystal forms.

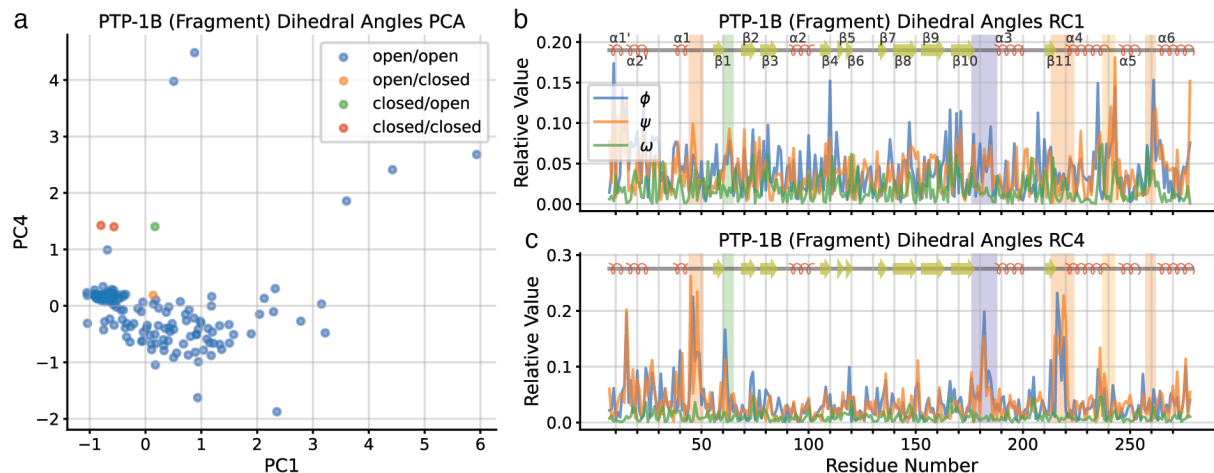


Figure S5: Additional dimensions of the PTP-1B conformational landscape inferred from crystallographic drug fragment screen structures.

(a) Fragment screen PTP-1B conformational landscape by dihedral angles, using PC1 and PC4. (b) Residue contributions to PC1, with active site loops in orange box, putative allosteric loop in dark blue box, WPD loop in purple box, and L16 loop in yellow box. (c) Residue contributions to PC4, with coloring as in panel (b).

574

575

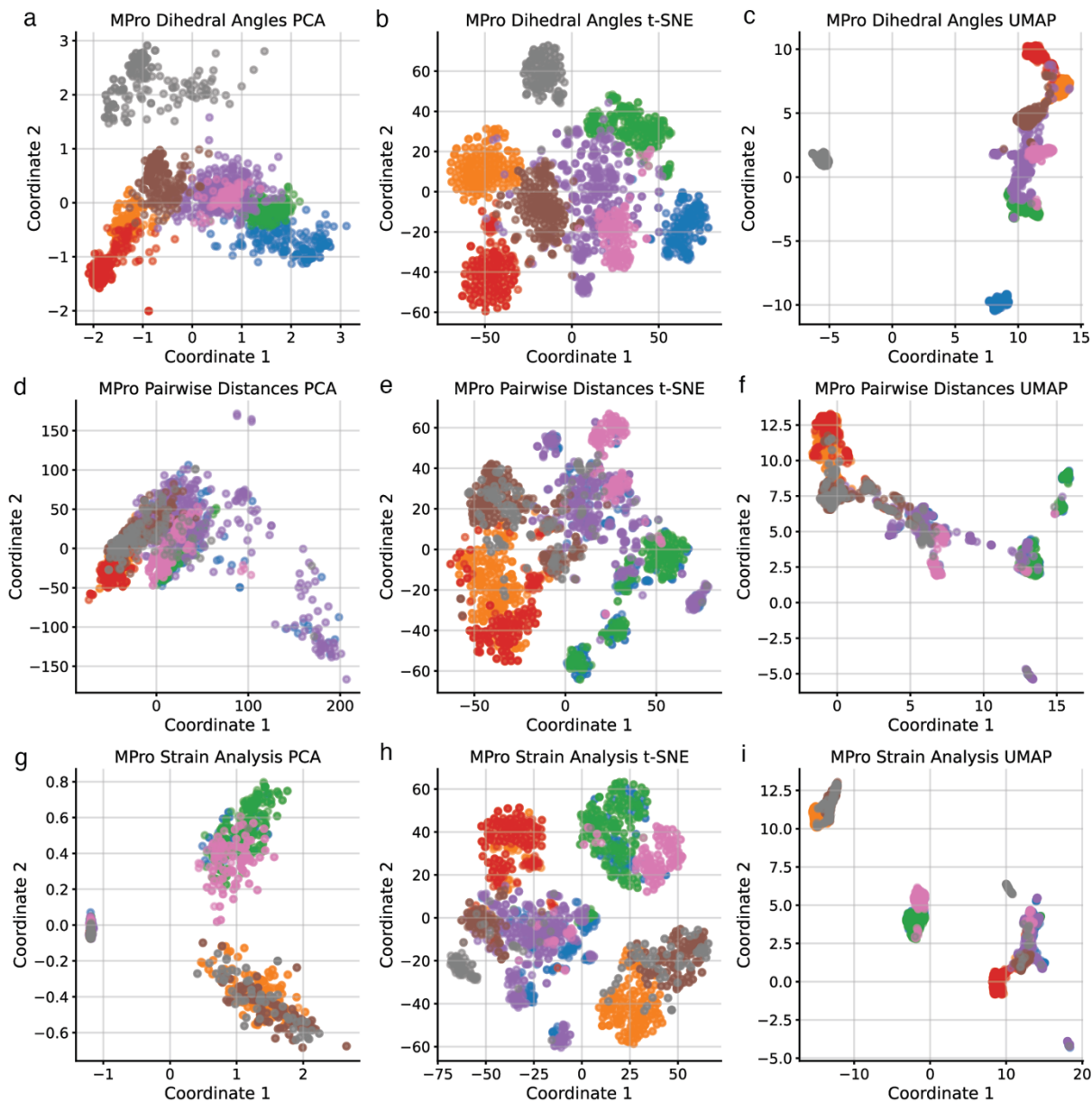


Figure S6: Comparison of PCA, t-SNE, and UMAP applied to all three structural representations of MPro.

(a-c) MPro conformational landscape based on dihedral angles with dimensionality reduction by (a) PCA, (b) t-SNE, and (c) UMAP. (d-f) MPro conformational landscape based on $C\alpha$ pairwise distances, analyzed using (d) PCA, (e) t-SNE, and (f) UMAP. (g-i) MPro conformational landscape based on strain analysis and (g) PCA, (h) t-SNE, and (i) UMAP. Coloring of structures is consistent among all panels.

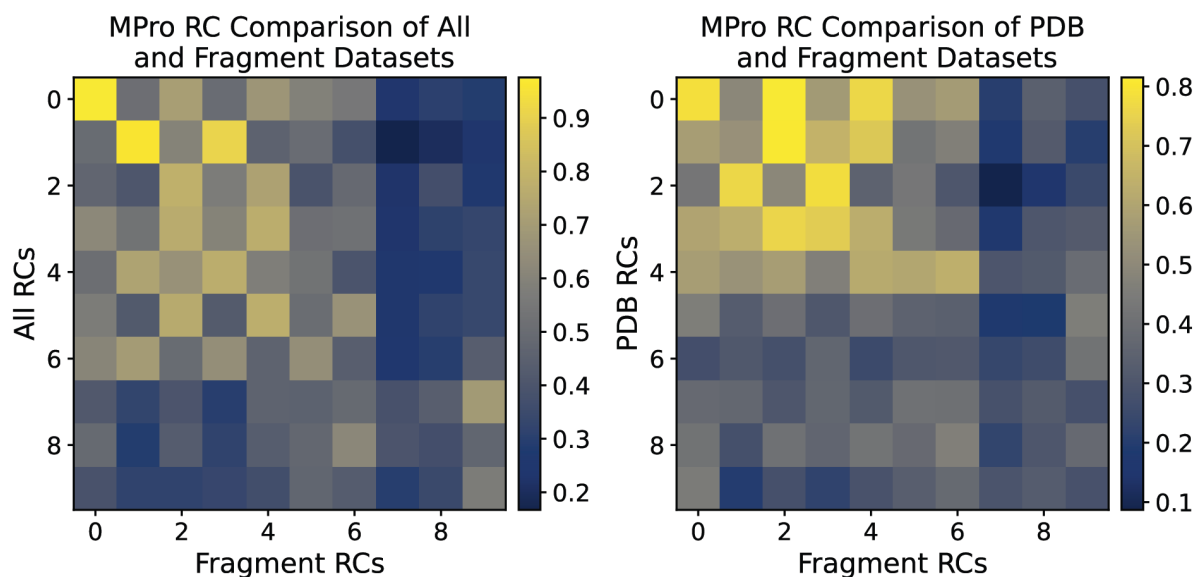


Figure S7: Comparison of dihedral angles residue contributions for MPro datasets.

(a) Correlation coefficient matrix comparing RCs of the complete MPro dataset to those of the fragment screen-only MPro dataset. (b) Correlation coefficient matrix comparing RCs of the PDB-only MPro dataset to those of the fragment screen-only MPro dataset.

578
579
580
581
582
583
584

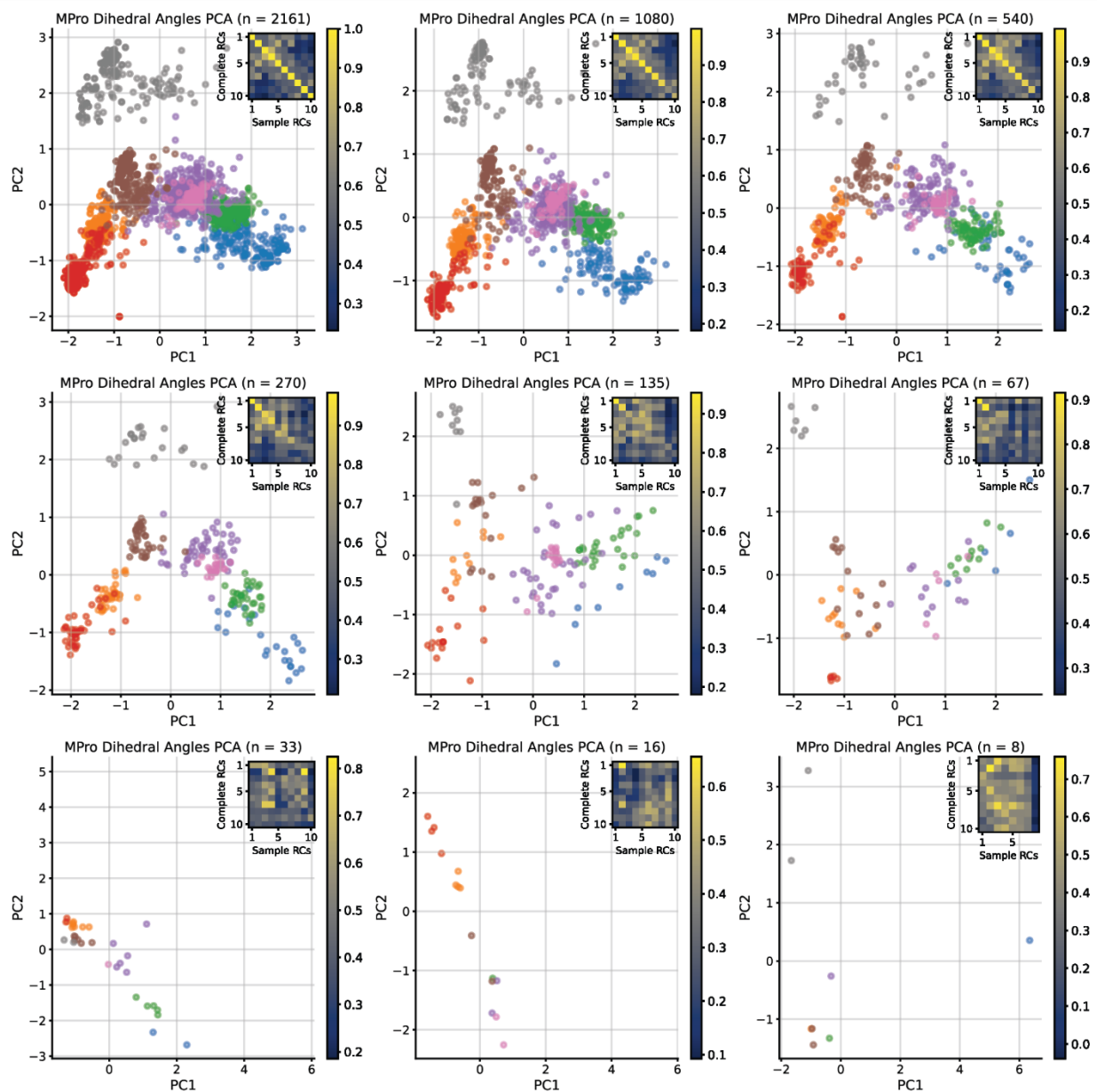


Figure S8: Effect of dataset size on the quality of inferred MPro conformational landscapes.

MPro conformational landscape by dihedral angles were determined for the complete dataset and subsampled datasets of $N = 2161$ (a), 1080 (b), 540 (c), 270 (d), 135 (e), 67 (f), 33 (g), 16 (h) or 8 (i) structures. In each panel we include an inset of the correlation of the residue contributions inferred for the complete dataset and the sampled dataset.

585

586

COLAV extract_data module			
Function	Parameters	Returns	Description
calculate_coverage_matching_scores	reference_strucs, sample_strucs, resnum_bounds, rmsd_threshold, verbose	coverage, matching	Calculates the coverage and matching metrics for a reference set of structures/conformational ensemble compared to a sample set of structures/conformational ensemble.
calculate_dh_t1	raw_dh_loading	transformed_dh_loading	Adjusts raw dihedral loading for interpretability.
calculate_pw_t1	raw_pw_loading, resnum_bounds	transformed_pw_loading	Adjusts raw pairwise distance loading for interpretability.
calculate_sa_t1	raw_sa_loading, shared_atom_list	transformed_sa_loading	Adjusts raw strain or shear loading for interpretability.
generate_dihedral_matrix	structure_list, resnum_bounds, no_psi, no_omega, no_phi, save, save_prefix, verbose	dh_data_matrix, dh_strucs	Extracts dihedral angles from given structures.
generate_pw_matrix	structure_list, resnum_bounds, save, save_prefix, verbose	pw_data_matrix, pw_strucs	Extracts pairwise distances from given structures.
generate_strain_matrix	structure_list, reference_pdb, data_type, resnum_bounds, atoms, alt_locs, save, save_prefix, save_additional, verbose	sa_data_matrix, sa_strucs	Extracts strain tensors, shear tensors, or shear energies from given structures.
load_dihedral_matrix	dh_pk1	dh_data_matrix, dh_strucs	Loads the dihedral data matrix and corresponding structures.
load_pw_matrix	pw_pk1	pw_data_matrix, pw_strucs	Loads the pairwise distance data matrix and corresponding structures.
load_strain_matrix	strain_pk1	sa_data_matrix, sa_strucs	Loads the strain data matrix and corresponding structures.

587
588 **Table S1: User-accessible COLAV functions for analyzing structural data.**
589 For a more complete description of the COLAV software package and its functionality, visit
590 <https://github.com/Hekstra-Lab/colav>. Note that “transformed loadings” are referred to in the text
591 as “residue contributions”.

592 **References**

- 593 1. Gao, S., and Klinman, J.P. (2022). Functional roles of enzyme dynamics in accelerating
594 active site chemistry: Emerging techniques and changing concepts. *Current Opinion in*
595 *Structural Biology* 75, 102434. <https://doi.org/10.1016/j.sbi.2022.102434>.
- 596 2. Henzler-Wildman, K., and Kern, D. (2007). Dynamic personalities of proteins. *Nature*
597 450, 964-972. 10.1038/nature06522.
- 598 3. Stachowski, T.R., and Fischer, M. (2022). Large-Scale Ligand Perturbations of the
599 Protein Conformational Landscape Reveal State-Specific Interaction Hotspots. *Journal of*
600 *Medicinal Chemistry* 65, 13692-13704. 10.1021/acs.jmedchem.2c00708.
- 601 4. Whittier, S.K., Hengge, A.C., and Loria, J.P. (2013). Conformational motions regulate
602 phosphoryl transfer in related protein tyrosine phosphatases. *Science* 341, 899-903.
603 10.1126/science.1241735.
- 604 5. Zuccotto, F., Ardini, E., Casale, E., and Angiolini, M. (2010). Through the “Gatekeeper
605 Door”: Exploiting the Active Kinase Conformation. *Journal of Medicinal Chemistry* 53,
606 2681-2694. 10.1021/jm901443h.
- 607 6. Greisman, J.B., Dalton, K.M., Brookner, D.B., Klureza, M.A., Sheehan, C.J., Kim, I.-S.,
608 Henning, R.W., Russi, S., and Hekstra, D.R. (2023). Resolving conformational changes
609 that mediate a two-step catalytic mechanism in a model enzyme. *bioRxiv*,
610 2023.2006.2002.543507. 10.1101/2023.06.02.543507.
- 611 7. Lewandowski, J.R., Halse, M.E., Blackledge, M., and Emsley, L. (2015). Direct
612 observation of hierarchical protein dynamics. *Science* 348, 578-581.
613 doi:10.1126/science.aaa6111.

- 614 8. Ramanathan, A., Savol, A., Burger, V., Chennubhotla, C.S., and Agarwal, P.K. (2014).
615 Protein Conformational Populations and Functionally Relevant Substates. *Accounts of*
616 *Chemical Research* 47, 149-156. 10.1021/ar400084s.
- 617 9. Noé, F., and Fischer, S. (2008). Transition networks for modeling the kinetics of
618 conformational change in macromolecules. *Current Opinion in Structural Biology* 18,
619 154-162. <https://doi.org/10.1016/j.sbi.2008.01.008>.
- 620 10. Juraszek, J., Vreede, J., and Bolhuis, P.G. (2012). Transition path sampling of protein
621 conformational changes. *Chemical Physics* 396, 30-44.
622 <https://doi.org/10.1016/j.chemphys.2011.04.032>.
- 623 11. Hekstra, D.R. (2023). Emerging Time-Resolved X-Ray Diffraction Approaches for
624 Protein Dynamics. *Annual Review of Biophysics* 52, 255-274. 10.1146/annurev-biophys-
625 111622-091155.
- 626 12. Alderson, T.R., and Kay, L.E. (2021). NMR spectroscopy captures the essential role of
627 dynamics in regulating biomolecular function. *Cell* 184, 577-595.
628 10.1016/j.cell.2020.12.034.
- 629 13. Mazal, H., and Haran, G. (2019). Single-molecule FRET methods to study the dynamics
630 of proteins at work. *Current Opinion in Biomedical Engineering* 12, 8-17.
631 <https://doi.org/10.1016/j.cobme.2019.08.007>.
- 632 14. McHaourab, H.S., Steed, P.R., and Kazmier, K. (2011). Toward the fourth dimension of
633 membrane protein structure: insight into dynamics from spin-labeling EPR spectroscopy.
634 *Structure* 19, 1549-1561. 10.1016/j.str.2011.10.009.
- 635 15. Fraser, J.S., van den Bedem, H., Samelson, A.J., Lang, P.T., Holton, J.M., Echols, N., and
636 Alber, T. (2011). Accessing protein conformational ensembles using room-temperature X-

- 637 ray crystallography. *Proceedings of the National Academy of Sciences* *108*, 16247-
638 16252. doi:10.1073/pnas.1111325108.
- 639 16. Elmlund, D., Le, S.N., and Elmlund, H. (2017). High-resolution cryo-EM: the nuts and
640 bolts. *Current Opinion in Structural Biology* *46*, 1-6.
641 <https://doi.org/10.1016/j.sbi.2017.03.003>.
- 642 17. Zhong, E.D., Bepler, T., Berger, B., and Davis, J.H. (2021). CryoDRGN: reconstruction
643 of heterogeneous cryo-EM structures using neural networks. *Nature Methods* *18*, 176-
644 185. 10.1038/s41592-020-01049-4.
- 645 18. Punjani, A., and Fleet, D.J. (2023). 3DFlex: determining structure and motion of flexible
646 proteins from cryo-EM. *Nature Methods* *20*, 860-870. 10.1038/s41592-023-01853-8.
- 647 19. Luo, Y., Pfuetzner, R.A., Mosimann, S., Paetzel, M., Frey, E.A., Cherney, M., Kim, B.,
648 Little, J.W., and Strynadka, N.C.J. (2001). Crystal Structure of LexA: A Conformational
649 Switch for Regulation of Self-Cleavage. *Cell* *106*, 585-594. 10.1016/S0092-
650 8674(01)00479-2.
- 651 20. Joerger, A.C., Allen, M.D., and Fersht, A.R. (2004). Crystal structure of a superstable
652 mutant of human p53 core domain. Insights into the mechanism of rescuing oncogenic
653 mutations. *J Biol Chem* *279*, 1291-1296. 10.1074/jbc.M309732200.
- 654 21. Wittinghofer, A., and Pal, E.F. (1991). The structure of Ras protein: a model for a
655 universal molecular switch. *Trends in Biochemical Sciences* *16*, 382-387. 10.1016/0968-
656 0004(91)90156-P.
- 657 22. Kondrashov, D.A., Zhang, W., Aranda IV, R., Stec, B., and Phillips Jr., G.N. (2008).
658 Sampling of the native conformational ensemble of myoglobin via structures in different

- 659 crystalline environments. *Proteins: Structure, Function, and Bioinformatics* 70, 353-362.
- 660 <https://doi.org/10.1002/prot.21499>.
- 661 23. Buerger, H.B., and Dunitz, J.D. (1983). From crystal statics to chemical dynamics.
- 662 *Accounts of Chemical Research* 16, 153-161. 10.1021/ar00089a002.
- 663 24. Douangamath, A., Powell, A., Fearon, D., Collins, P.M., Talon, R., Krojer, T., Skyner, R.,
- 664 Brandao-Neto, J., Dunnett, L., Dias, A., et al. (2021). Achieving Efficient Fragment
- 665 Screening at XChem Facility at Diamond Light Source. *JoVE*, e62414.
- 666 doi:10.3791/62414.
- 667 25. Pearce, N.M., Krojer, T., Bradley, A.R., Collins, P., Nowak, R.P., Talon, R., Marsden,
- 668 B.D., Kelm, S., Shi, J., Deane, C.M., and von Delft, F. (2017). A multi-crystal method for
- 669 extracting obscured crystallographic states from conventionally uninterpretable electron
- 670 density. *Nature Communications* 8, 15123. 10.1038/ncomms15123.
- 671 26. Ginn, H. (2020). Pre-clustering data sets using cluster4x improves the signal-to-noise
- 672 ratio of high-throughput crystallography drug-screening analysis. *Acta Crystallographica*
- 673 *Section D* 76, 1134-1144. doi:10.1107/S2059798320012619.
- 674 27. Berman, H.M., Westbrook, J., Feng, Z., Gilliland, G., Bhat, T.N., Weissig, H.,
- 675 Shindyalov, I.N., and Bourne, P.E. (2000). The Protein Data Bank. *Nucleic Acids*
- 676 *Research* 28, 235-242. 10.1093/nar/28.1.235.
- 677 28. Harris, C.R., Millman, K.J., van der Walt, S.J., Gommers, R., Virtanen, P., Cournapeau,
- 678 D., Wieser, E., Taylor, J., Berg, S., Smith, N.J., et al. (2020). Array programming with
- 679 NumPy. *Nature* 585, 357-362. 10.1038/s41586-020-2649-2.
- 680 29. Virtanen, P., Gommers, R., Oliphant, T.E., Haberland, M., Reddy, T., Cournapeau, D.,
- 681 Burovski, E., Peterson, P., Weckesser, W., Bright, J., et al. (2020). *SciPy 1.0: fundamental*

- 682 algorithms for scientific computing in Python. *Nature Methods* *17*, 261-272.
683 10.1038/s41592-019-0686-2.
- 684 30. Raschka, S. (2017). BioPandas: Working with molecular structures in pandas
685 DataFrames. *Journal of Open Source Software* *2*, 279. 10.21105/joss.00279.
- 686 31. Gullett, P.M., Horstemeyer, M.F., Baskes, M.I., and Fang, H. (2007). A deformation
687 gradient tensor and strain tensors for atomistic simulations. *Modelling and Simulation in*
688 *Materials Science and Engineering* *16*, 015001. 10.1088/0965-0393/16/1/015001.
- 689 32. Mitchell, M.R., Tlusty, T., and Leibler, S. (2016). Strain analysis of protein structures and
690 low dimensionality of mechanical allosteric couplings. *Proc Natl Acad Sci U S A* *113*,
691 E5847-E5855. 10.1073/pnas.1609462113.
- 692 33. Pedregosa, F., Varoquaux, G., Gramfort, A., Michel, V., Thirion, B., Grisel, O., Blondel,
693 M., Prettenhofer, P., Weiss, R., Dubourg, V., et al. (2011). Scikit-learn: Machine Learning
694 in Python. *Journal of Machine Learning Research* *12*, 2825-2830.
- 695 34. Van der Maaten, L., and Hinton, G. (2008). Visualizing data using t-SNE. *Journal of*
696 *machine learning research* *9*.
- 697 35. McInnes, L., Healy, J., and Melville, J. (2018). UMAP: Uniform Manifold
698 Approximation and Projection for Dimension Reduction. *arXiv*.
699 10.48550/ARXIV.1802.03426.
- 700 36. Keedy, D.A., Hill, Z.B., Biel, J.T., Kang, E., Rettenmaier, T.J., Brandao-Neto, J., Pearce,
701 N.M., von Delft, F., Wells, J.A., and Fraser, J.S. (2018). An expanded allosteric network
702 in PTP1B by multitemperature crystallography, fragment screening, and covalent
703 tethering. *Elife* *7*. 10.7554/eLife.36307.

- 704 37. Douangamath, A., Fearon, D., Gehrtz, P., Krojer, T., Lukacik, P., Owen, C.D., Resnick,
705 E., Strain-Damerell, C., Aimon, A., Ábrányi-Balogh, P., et al. (2020). Crystallographic
706 and electrophilic fragment screening of the SARS-CoV-2 main protease. *Nature*
707 *Communications* 11, 5047. [10.1038/s41467-020-18709-w](https://doi.org/10.1038/s41467-020-18709-w).
- 708 38. Zhang, C.-H., Stone, E.A., Deshmukh, M., Ippolito, J.A., Ghahremanpour, M.M., Tirado-
709 Rives, J., Spasov, K.A., Zhang, S., Takeo, Y., Kudalkar, S.N., et al. (2021). Potent
710 Noncovalent Inhibitors of the Main Protease of SARS-CoV-2 from Molecular Sculpting
711 of the Drug Perampanel Guided by Free Energy Perturbation Calculations. *ACS Central*
712 *Science* 7, 467-475. [10.1021/acscentsci.1c00039](https://doi.org/10.1021/acscentsci.1c00039).
- 713 39. Qiao, J., Li, Y.-S., Zeng, R., Liu, F.-L., Luo, R.-H., Huang, C., Wang, Y.-F., Zhang, J.,
714 Quan, B., Shen, C., et al. (2021). SARS-CoV-2 Mpro inhibitors with antiviral activity in a
715 transgenic mouse model. *Science* 371, 1374-1378. [10.1126/science.abf1611](https://doi.org/10.1126/science.abf1611).
- 716 40. Noske, G.D., Nakamura, A.M., Gawriljuk, V.O., Fernandes, R.S., Lima, G.M.A., Rosa,
717 H.V.D., Pereira, H.D., Zeri, A.C.M., Nascimento, A.F.Z., Freire, M.C.L.C., et al. (2021).
718 A Crystallographic Snapshot of SARS-CoV-2 Main Protease Maturation Process. *Journal*
719 *of Molecular Biology* 433, 167118. <https://doi.org/10.1016/j.jmb.2021.167118>.
- 720 41. Günther, S., Reinke, P.Y.A., Fernández-García, Y., Lieske, J., Lane, T.J., Ginn, H.M.,
721 Koua, F.H.M., Ehrt, C., Ewert, W., Oberthuer, D., et al. (2021). X-ray screening identifies
722 active site and allosteric inhibitors of SARS-CoV-2 main protease. *Science* 372, 642-646.
723 [10.1126/science.abf7945](https://doi.org/10.1126/science.abf7945).
- 724 42. Ebrahim, A., Riley, B.T., Kumaran, D., Andi, B., Fuchs, M.R., McSweeney, S., and
725 Keedy, D.A. (2022). The temperature-dependent conformational ensemble of SARS-
726 CoV-2 main protease (Mpro). *IUCrJ* 9, 682-694. [doi:10.1107/S2052252522007497](https://doi.org/10.1107/S2052252522007497).

- 727 43. Wojdyr, M. (2022). GEMMI: A library for structural biology. *Journal of Open Source*
728 *Software* 7, 4200. [10.21105/joss.04200](https://doi.org/10.21105/joss.04200).
- 729 44. Theobald, D.L., and Wuttke, D.S. (2006). THESEUS: maximum likelihood
730 superpositioning and analysis of macromolecular structures. *Bioinformatics* 22, 2171-
731 2172. [10.1093/bioinformatics/btl332](https://doi.org/10.1093/bioinformatics/btl332).
- 732 45. Ginn, H.M. (2022). Torsion angles to map and visualize the conformational space of a
733 protein. *bioRxiv*, 2022.2008.2004.502807. [10.1101/2022.08.04.502807](https://doi.org/10.1101/2022.08.04.502807).
- 734 46. Elchebly, M., Payette, P., Michaliszyn, E., Cromlish, W., Collins, S., Loy, A.L.,
735 Normandin, D., Cheng, A., Himms-Hagen, J., Chan, C.C., et al. (1999). Increased insulin
736 sensitivity and obesity resistance in mice lacking the protein tyrosine phosphatase-1B
737 gene. *Science* 283, 1544-1548. [10.1126/science.283.5407.1544](https://doi.org/10.1126/science.283.5407.1544).
- 738 47. Krishnan, N., Koveal, D., Miller, D.H., Xue, B., Akshinthala, S.D., Kragelj, J., Jensen,
739 M.R., Gauss, C.M., Page, R., Blackledge, M., et al. (2014). Targeting the disordered C
740 terminus of PTP1B with an allosteric inhibitor. *Nat Chem Biol* 10, 558-566.
741 [10.1038/nchembio.1528](https://doi.org/10.1038/nchembio.1528).
- 742 48. Konrad, M.R., Shelly, A.C., Zhaohong, Q., Kaveh, F., Fariba, S., Li, Z., Michael, A.Z.,
743 Alexandre, F.R.S., and Hsiao-Huei, C. (2020). Neuronal Protein Tyrosine Phosphatase 1B
744 Hastens Amyloid β -Associated Alzheimer's Disease in Mice. *The Journal of*
745 *Neuroscience* 40, 1581. [10.1523/JNEUROSCI.2120-19.2019](https://doi.org/10.1523/JNEUROSCI.2120-19.2019).
- 746 49. Liu, R., Mathieu, C., Berthelet, J., Zhang, W., Dupret, J.M., and Rodrigues Lima, F.
747 (2022). Human Protein Tyrosine Phosphatase 1B (PTP1B): From Structure to Clinical
748 Inhibitor Perspectives. *Int J Mol Sci* 23. [10.3390/ijms23137027](https://doi.org/10.3390/ijms23137027).

- 749 50. Andersen, J.N., and Tonks, N.K. (2004). Protein tyrosine phosphatase-based therapeutics:
750 lessons from PTP1B. In *Protein Phosphatases*, J.n. Ariño, and D.R. Alexander, eds.
751 (Springer Berlin Heidelberg), pp. 201-230. 10.1007/978-3-540-40035-6_11.
- 752 51. Zhang, Z.Y. (2017). Drugging the Undruggable: Therapeutic Potential of Targeting
753 Protein Tyrosine Phosphatases. *Acc Chem Res* 50, 122-129.
754 10.1021/acs.accounts.6b00537.
- 755 52. Wiesmann, C., Barr, K.J., Kung, J., Zhu, J., Erlanson, D.A., Shen, W., Fahr, B.J., Zhong,
756 M., Taylor, L., Randal, M., et al. (2004). Allosteric inhibition of protein tyrosine
757 phosphatase 1B. *Nat Struct Mol Biol* 11, 730-737. 10.1038/nsmb803.
- 758 53. Choy, M.S., Li, Y., Machado, L., Kunze, M.B.A., Connors, C.R., Wei, X., Lindorff-
759 Larsen, K., Page, R., and Peti, W. (2017). Conformational Rigidity and Protein Dynamics
760 at Distinct Timescales Regulate PTP1B Activity and Allostery. *Mol Cell* 65, 644-658
761 e645. 10.1016/j.molcel.2017.01.014.
- 762 54. Cui, D.S., Beaumont, V., Ginther, P.S., Lipchock, J.M., and Loria, J.P. (2017). Leveraging
763 Reciprocity to Identify and Characterize Unknown Allosteric Sites in Protein Tyrosine
764 Phosphatases. *J Mol Biol* 429, 2360-2372. 10.1016/j.jmb.2017.06.009.
- 765 55. Popovych, N., Sun, S., Ebright, R.H., and Kalodimos, C.G. (2006). Dynamically driven
766 protein allostery. *Nature Structural & Molecular Biology* 13, 831-838.
767 10.1038/nsmb1132.
- 768 56. Venkitakrishnan, R.P., Zaborowski, E., McElheny, D., Benkovic, S.J., Dyson, H.J., and
769 Wright, P.E. (2004). Conformational Changes in the Active Site Loops of Dihydrofolate
770 Reductase during the Catalytic Cycle. *Biochemistry* 43, 16046-16055.
771 10.1021/bi048119y.

- 772 57. Petit, C.M., Zhang, J., Sapienza, P.J., Fuentes, E.J., and Lee, A.L. (2009). Hidden
773 dynamic allostery in a PDZ domain. *Proceedings of the National Academy of Sciences*
774 *106*, 18249-18254. [10.1073/pnas.0904492106](https://doi.org/10.1073/pnas.0904492106).
- 775 58. Pohl, F.M. (1971). Empirical Protein Energy Maps. *Nature New Biology* *234*, 277-279.
776 [10.1038/newbio234277a0](https://doi.org/10.1038/newbio234277a0).
- 777 59. Miyazawa, S., and Jernigan, R.L. (1985). Estimation of effective interresidue contact
778 energies from protein crystal structures: quasi-chemical approximation. *Macromolecules*
779 *18*, 534-552. [10.1021/ma00145a039](https://doi.org/10.1021/ma00145a039).
- 780 60. Godzik, A. (1996). Knowledge-based potentials for protein folding: what can we learn
781 from known protein structures? *Structure* *4*, 363-366. [10.1016/s0969-2126\(96\)00041-x](https://doi.org/10.1016/s0969-2126(96)00041-x).
- 782 61. Dunbrack, R.L., Jr., and Cohen, F.E. (1997). Bayesian statistical analysis of protein side-
783 chain rotamer preferences. *Protein Sci* *6*, 1661-1681. [10.1002/pro.5560060807](https://doi.org/10.1002/pro.5560060807).
- 784 62. Jumper, J., Evans, R., Pritzel, A., Green, T., Figurnov, M., Ronneberger, O.,
785 Tunyasuvunakool, K., Bates, R., Žídek, A., Potapenko, A., et al. (2021). Highly accurate
786 protein structure prediction with AlphaFold. *Nature* *596*, 583-589. [10.1038/s41586-021-](https://doi.org/10.1038/s41586-021-03819-2)
787 [03819-2](https://doi.org/10.1038/s41586-021-03819-2).
- 788 63. Roney, J.P., and Ovchinnikov, S. (2022). State-of-the-Art Estimation of Protein Model
789 Accuracy Using AlphaFold. *Physical Review Letters* *129*, 238101.
790 [10.1103/PhysRevLett.129.238101](https://doi.org/10.1103/PhysRevLett.129.238101).
- 791 64. van Montfort, R.L.M., Congreve, M., Tisi, D., Carr, R., and Jhoti, H. (2003). Oxidation
792 state of the active-site cysteine in protein tyrosine phosphatase 1B. *Nature* *423*, 773-777.
793 [10.1038/nature01681](https://doi.org/10.1038/nature01681).

- 794 65. Salmeen, A., Andersen, J.N., Myers, M.P., Meng, T.-C., Hinks, J.A., Tonks, N.K., and
795 Barford, D. (2003). Redox regulation of protein tyrosine phosphatase 1B involves a
796 sulphenyl-amide intermediate. *Nature* 423, 769-773. [10.1038/nature01680](https://doi.org/10.1038/nature01680).
- 797 66. Barrett, W.C., DeGnore, J.P., König, S., Fales, H.M., Keng, Y.-F., Zhang, Z.-Y., Yim,
798 M.B., and Chock, P.B. (1999). Regulation of PTP1B via Glutathionylation of the Active
799 Site Cysteine 215. *Biochemistry* 38, 6699-6705. [10.1021/bi990240v](https://doi.org/10.1021/bi990240v).
- 800 67. Netto, L.E.S., and Machado, L.E.S.F. (2022). Preferential redox regulation of cysteine-
801 based protein tyrosine phosphatases: structural and biochemical diversity. *The FEBS*
802 *Journal* 289, 5480-5504. <https://doi.org/10.1111/febs.16466>.
- 803 68. Yang, C.-Y., Yang, C.-F., Tang, X.-F., Machado, L.E.S.F., Singh, J.P., Peti, W., Chen, C.-
804 S., and Meng, T.-C. (2023). Active-site cysteine 215 sulfonation targets protein tyrosine
805 phosphatase PTP1B for Cullin1 E3 ligase-mediated degradation. *Free Radical Biology*
806 *and Medicine* 194, 147-159. <https://doi.org/10.1016/j.freeradbiomed.2022.11.041>.
- 807 69. Ravichandran, L.V., Chen, H., Li, Y., and Quon, M.J. (2001). Phosphorylation of PTP1B
808 at Ser50 by Akt Impairs Its Ability to Dephosphorylate the Insulin Receptor. *Molecular*
809 *Endocrinology* 15, 1768-1780. [10.1210/mend.15.10.0711](https://doi.org/10.1210/mend.15.10.0711).
- 810 70. Bandyopadhyay, D., Kusari, A., Kenner, K.A., Liu, F., Chernoff, J., Gustafson, T.A., and
811 Kusari, J. (1997). Protein-Tyrosine Phosphatase 1B Complexes with the Insulin Receptor
812 in Vivo and Is Tyrosine-phosphorylated in the Presence of Insulin*. *Journal of Biological*
813 *Chemistry* 272, 1639-1645. <https://doi.org/10.1074/jbc.272.3.1639>.
- 814 71. Cimermancic, P., Weinkam, P., Rettenmaier, T.J., Bichmann, L., Keedy, D.A., Woldeyes,
815 R.A., Schneidman-Duhovny, D., Demerdash, O.N., Mitchell, J.C., Wells, J.A., et al.
816 (2016). CryptoSite: Expanding the Druggable Proteome by Characterization and

- 817 Prediction of Cryptic Binding Sites. *J Mol Biol* 428, 709-719.
818 10.1016/j.jmb.2016.01.029.
- 819 72. Shi, C., Luo, S., Xu, M., and Tang, J. (2021). Learning Gradient Fields for Molecular
820 Conformation Generation. *CoRR abs/2105.03902*.
- 821 73. Xu, M., Luo, S., Bengio, Y., Peng, J., and Tang, J. (2021). Learning Neural Generative
822 Dynamics for Molecular Conformation Generation. *CoRR abs/2102.10240*.
- 823 74. V'kovski, P., Kratzel, A., Steiner, S., Stalder, H., and Thiel, V. (2021). Coronavirus
824 biology and replication: implications for SARS-CoV-2. *Nature Reviews Microbiology*
825 19, 155-170.
- 826 75. Fan, K., Wei, P., Feng, Q., Chen, S., Huang, C., Ma, L., Lai, B., Pei, J., Liu, Y., and Chen,
827 J. (2004). Biosynthesis, purification, and substrate specificity of severe acute respiratory
828 syndrome coronavirus 3C-like proteinase. *Journal of Biological Chemistry* 279, 1637-
829 1642.
- 830 76. Goyal, B., and Goyal, D. (2020). Targeting the Dimerization of the Main Protease of
831 Coronaviruses: A Potential Broad-Spectrum Therapeutic Strategy. *ACS Combinatorial*
832 *Science* 22, 297-305. 10.1021/acscombsci.0c00058.
- 833 77. Weng, Y.L., Naik, S.R., Dingelstad, N., Lugo, M.R., Kalyanamoorthy, S., and Ganesan,
834 A. (2021). Molecular dynamics and in silico mutagenesis on the reversible inhibitor-
835 bound SARS-CoV-2 main protease complexes reveal the role of lateral pocket in
836 enhancing the ligand affinity. *Scientific Reports* 11, 7429. 10.1038/s41598-021-86471-0.
837